Ensemble averaged structure-function relationship for composite nanocrystals: magnetic bcc Fe clusters with catalytically active fcc Pt skin

Valeri Petkov,[1] Binay Prasai,[1] Sarvjit Shastri,[2] Hyun-Uk Park,[3] Young-Uk Kwon [3] and Vassil Skumryev [4]

[1]Department of Physics, Central Michigan University, Mt. Pleasant, Michigan 48859, United States
[2]X-ray Science Division, Advanced Photon Source, Argonne National Laboratory, Argonne, Illinois 60439, United States
[3]Department of Chemistry, Sungkyunkwan University, Suwan 16419, Republic of Korea
[4]Department of Physics, Universitat Autònoma de Barcelona, Bellateria 08913, Spain

The three-dimensional (3D) atomic structure of a bulk crystal is perfectly periodic over long-range (μm-sized) distances and so its physicochemical properties come as a sum of equivalent contributions of identical unit cells comprising a relatively small number of atoms. The 3D atomic structure of a nanometer-sized crystal (NC) though is not necessarily perfectly periodic. Hence, the properties of a NC often appear as a convolution of the contributions of structurally incoherent volume fractions of the NC such as, for example, the NC surface and interior. Furthermore, reality necessitates the production, characterization and usage of NCs en masse. No matter how refined is the production process, the 3D atomic structure and properties of some NCs from the general population would appear more-or-less different from those of the rest [1-3]. On a related matter, theory on structure dependent properties of NCs relies heavily on model structures borrowed from bulk crystals, thereby remaining largely constrained within the realms of traditional crystallography [4, 5]. Undoubtedly, both taking control over the physicochemical properties of NCs and unleashing the predictive power of pertinent theory require precise atomic-level knowledge of the inherently non-3D periodic NCs, as they are produced and used in large numbers. Most relevant is knowledge of the ensemble-averaged positions of atoms in the NCs because the functionality of NCs also appears as an ensemble-averaged quantity.

Despite recent advances in techniques for atomic-level characterization of crystalline materials, determining the 3D atomic structure and so establishing the structure-function relationship for NCs, in particular metallic NCs, remains a problem [6-8]. Traditional crystallography is of little help because metallic NCs do not conform to its methodology. Besides, due to their dual cluster-solid bulk nature or by deliberate design, metallic NCs often adopt an uncommon atomic structure, including an incommensurately modulated and composite

nanostructure. Here we determine the ensemble-averaged 3D atomic structure of three samples of 2.5 nm in size NCs composed of a Fe core nested inside Pt skin. The cores comprise from 160 to 330 atoms and so may be considered cluster-like. The skin involves from one to two atomic layers alone, i.e. is super-thin. The samples are tailored for practical applications and so appear as ensembles of a very large number of NCs. The structure determination is done by resonant high-energy x-ray diffraction (HE-XRD) coupled to atomic pair distribution function (PDF) analysis that does not imply long-range order and periodicity [9]. We find that the core and skin are bcc- and fcc-type ordered, respectively, i.e. incommensurate in terms of packing efficiency and near neighbor distribution. Regardless, they modulate the properties of each other significantly and advantageously. In particular, the NCs function both as superparamagnets and exceptional catalysts for the oxygen reduction reaction (ORR). The former holds promise for advanced biomedical applications [10,11]. The latter is crucial to the development of efficient devices for clean energy conversion such as fuel cells [12]. Using 3D positions of atoms in the NCs together with experimental magnetic and catalytic data, not only we capture but also quantify both the long-time debated cluster-size dependence of the magnetic moment of Fe atoms and impact of Pt skin-thickness on the activity of ORR catalysts. Thus we demonstrate that knowledge of NC ensemble-averaged 3D atomic positions is indispensable in revealing the structure-function relationship for ensembles of NCs.

The Fe core-Pt skin NCs were synthesized by one step ultrasound-assisted polyol reactions between Fe(III) acetylacetonate, $Fe(C_5H_7O_2)_3$, and Pt(II) acetylacetonate, $Pt(C_5H_7O_2)_2$ [13]. The size of Fe core and thickness of Pt skin were fine-tuned through varying the $Fe(C_5H_7O_2)_3$ to $Pt(C_5H_7O_2)_2$ ratio so that the overall size of resultant NCs was kept close to 2.5 nm. Pure Pt NCs were also synthesized and used as a standard in the 3D structure determination. Note that Pt-based NCs with a size close to 3 nm have proven optimal for a number of technologically important catalytic applications, including ORR. Besides, biocompatible and oxidation resistant, e.g. noble metal protected, superparamagnetic particles with an overall size of about 2-3 nm can interact with common biological entities, including genes (~ 2 nm), protein complexes (1 nm–5 nm) and cell's membrane (~5 nm), thereby enabling cellular therapy, magnetically-guided drug delivery, magnetic resonance imaging, and hyperthermia treatment [14]. More details of the synthesis protocol employed here can be found in the Methods section of supplementary information (SI).

The overall (bulk) chemical composition of Fe core-Pt skin NCs was determined by inductively coupled plasma atomic emission spectroscopy (ICP-AES) and found to be $Fe_{0.4}Pt$ ($Fe_{166}Pt_{421}$), $Fe_{0.7}Pt$ ($Fe_{244}Pt_{351}$) and $Fe_{1.2}Pt$ ($Fe_{363}Pt_{297}$). The size, shape and chemical pattern of Fe_xPt (x=0.4, 0.7 and 1.2) NCs were determined by High-Angle Annular Dark-Field (HAADF) Scanning Transition Electron Microscopy (STEM) experiments. Exemplary HAADF-STEM images are shown in Figures 1*b* and S1. As can be seen in the Figures, pure Pt and Fe_xPt (x=0.4, 0.7 and 1.2) NCs are rather uniform in terms of size and shape.To be more specific, the NCs appear with an average size of 2.5(± 0.2) nm, polyhedral shape, and well-defined facets. Besides, the NCs are well separated from each other which is important for optimizing their functionality. Furthermore, a closer inspection of the images in Figure 1 reveals that the NCs exhibit well-defined lattice fringes, i.e. exhibit a relatively low degree of local structural disorder. In addition, the surface of NCs appears uniformly bright which, given the disparity between the atomic numbers of Fe (Z=26) and Pt (Z=78), indicates that the top surface layer of the NCs is formed of Pt species alone. Elemental maps of Fe_xPt (x=0.4. 07 and 1.2) NPs are shown in Figure 1(*d*, *e* and *f*). The maps also indicate that Fe and Pt atoms occupy the NC core and surface, respectively. To evaluate the number of surface Pt layers we carried out simplistic calculations based on the experimental data for the bulk chemical composition and average size of the NCs, and the elemental size of Fe (2.52) Å and Pt (2.775 Å) atoms. Results showed that Pt surface of Fe_xPt (x=0.4, 0.7 and 1.2) NPs is two, one and a half and one atomic layer thick, respectively, i.e., from a morphological point of view, is "skin-like". The so-obtained independent estimates for the thickness of Pt skin matched well the pre-desired number of Pt layers. Hence, for clarity, hereafter Fe_xPt (x=0.4, 0.7 and 1.2) NCs will be referred to as Fe@2Pt, Fe@1.5Pt and Fe@1Pt NCs, respectively.

The electronic properties of Fe and Pt atoms in Fe@Pt NCs were studied by x-ray photoelectron spectroscopy (XPS). Typical XPS Fe *2p* and Pt 4*f* spectra are shown in Figure 1*a*. As can be seen in the Figure, the Fe $2p_{3/2}$ core-level peak position in Fe@1Pt, Fe@1.5Pt and Fe@2Pt NCs is shifted by 0.59 eV, 0.79 eV and 1.19 eV, respectively, in comparison to the bulk value of 706.9 eV. As discussed in the Method section of SI and supported by independent resonant HE-XRD experiments (see Figure S7), the shift is unlikely to arise from oxidation of Fe cores. Rather, as also demonstrated by data in Figures 1(*d*,*e*,*f*) and 2*d*, it reflects the gradual diminishing of the size of Fe cores with the thickness of Pt skin [15]. On the other hand, the Pt

$4f_{7/2}$ core-level peak position in Fe@1Pt, Fe@1.5Pt and Fe@2Pt NCs is shifted by -0.34 eV, -0.25 eV and -0.12 eV, respectively, in comparison to the bulk value of 71.0 eV (see Figure 1c). As discussed in the Methods secton of SI, the shift may not be due to the presence of PtO_x species. Besides, the shift may not be due to the formation of surface Fe-Pt alloy either because prior studies have shown that Pt $4f_{7/2}$ orbitals in Pt-Fe nanoalloys shift up in energy by about 0.5 eV [16]. Below, we argue that the observed shifts in the Fe $2p_{3/2}$ and Pt $4f_{7/2}$ core-level peak position are likely to arise from concurrent changes in the surface Fe-Fe and Pt-Pt coordination numbers (CNs) with the size of Fe cores and thickness of Pt skin, respectively [17-19].

Ensemble-averaged 3D positions of atoms in Fe@Pt NCs were determined strictly adhering to the successful practices of structure studies on polycrystalline metallic materials [20]. From a methodological point of view, this made perfect sense because determining the 3D atomic structure of both polycrystalline and nanocrystalline metallic particles relies on diffraction data obtained from ensembles of entities with a fairly close chemical composition, size, and shape [20]. In particular, resonant HE-XRD experiments were conducted at the K adsorption edge of Pt (see Figure S4). The experiments involved measuring two diffraction patterns close to but below the adsorption edge of Pt, taking the difference between the two patterns, and Fourier transforming the difference into the so-called Pt-differential PDFs. The so-called total and Fe-Fe partial PDFs were also obtained. The PDFs are summarized in Figure 2. More details of the resonant HE-XRD experiments and derivation of total, differential and partial atomic PDFs can be found in the Methods section of SI. Note that unlike local-probe techniques such as extended x-ray absorption fine structure spectroscopy (EXAFS), element-specific atomic PDFs obtained by resonant HE-XRD can reveal interatomic correlations extending up to distances equal to the diameter (size) of the metallic NCs under study. For instance, as data in Figure 2*d* show (see broken line), Fe-Fe partial PDFs extend up to distances close to the size of respective Fe cores. Total atomic PDFs for 2.5 nm Pt and 4.5 nm Fe particles [22] were also obtained by HE-XRD. The quality of resonant HE-XRD experiments was crosschecked by measuring bulk Fe and Pt standards and affirmed as shown in Figure 2*b*.

Next, several plausible 3D structure models for Fe@Pt NCs were built by Molecular Dynamics (MD) based on the quantum corrected Sutton-Chen potential. To be as realistic as possible, the models reflected the average size (~2.5 nm), shape (polyhedral) and overall chemical composition (Fe_xPt, where x=0.4. 07 and 1.2) of the NCs modeled. Models for pure Pt

and Fe particles were also built. All models were tested against the respective total and Fe-Fe partial PDFs. As discussed in the Methods section of SI and demonstrated in Figure S8, MD models featuring an fcc and bcc-type structure approached the experimental PDFs for pure Pt and Fe particles to an acceptable level, and so were considered further. However, MD models for Fe@Pt NCs based on a structurally coherent fcc Fe core and fcc Pt shell failed the test, as data in Figures 2*a* and S9 show. The failure indicated that, though exhibiting HE-XRD patterns similar to that of pure Pt particles, (see Figure S3), Fe@Pt NCs may not be described as stacks of close packed atomic layers known to occur with bulk fcc metals and alloys, including bulk Pt and Fe_xPt alloys with $0<x<1.2$ [23]. On the other hand, as data in Figures 2*a* and S10 show, models for Fe@Pt NCs based on a bcc Fe core and fcc Pt skin reproduced the experimental PDF data reasonably well. For reference, contrary to the fcc-type structure, which involves both close packed $(111)_{fcc}$ atomic layers and $<110>_{fcc}$ directions, the bcc-type structure does not involve close packed atomic layers but close packed $<111>_{bcc}$ directions alone [24]. Accordingly, the atomic packing fraction (68 % for bcc vs 74 % for fcc) and near-neighbor distribution (8 + 6 for bcc vs 12 for fcc; see Figure 2*b*) in the bcc- and fcc-type structure are significantly different. The advantage of bcc-Fe@fcc-Pt structure model over the fcc-Fe@fcc-Pt one becomes even more evident when Fe-Fe partial PDFs derived from the models are compared with the respective experimental data sets, as demonstrated in Figure S11. Hence, the former model was considered as a likely 3D atomic structure of Fe@Pt NCs. Here it may be added that the bcc and fcc character of the atomic arrangement in Fe cores and Pt skin, respectively, is consistent with the synthesis protocol adopted here, where Pt atoms are deposited on already formed cores of Fe atoms.

Third, MD models for Fe@Pt NCs found likely as described above were refined further by reverse Monte Carlo (RMC) guided by the respective total and partial Fe-Fe atomic PDFs. The bcc- and fcc-type structure models for pure Fe and Pt particles were refined as well. The refinement was necessary since nanosized metallic particles can exhibit specific structural features, such as considerable surface relaxation, which may not be captured well by MD alone, i.e. without experimental input [25]. As it should be, the thermal (Debye−Waller type) and static displacements, i.e. relaxation, of atoms in the refined models were treated separately. Besides, the energy of refined models was minimized further using pair-wise potentials taken from literature sources. Details of RMC computations can be found in the Methods section of SI.

Last but not least, RMC-refined models were evaluated using a common goodness-or-fit indicator (see *eq. S26*) and found of high quality. Fine structural features of Fe cores and Pt skin in Fe@Pt NCs were cross-checked by computing bond-angle distributions, shown in Figures S13 and S14. The distributions confirmed the bcc- and fcc-type 3D structure of the former and latter, respectively. Altogether, the RMC-refined models appeared fully consistent with the i) experimental HAADF-STEM data in terms of size and shape, ii) EDS maps in terms of mutual distribution of Fe and Pt atoms, iii) ACP-IES data in terms of overall chemical composition and, as shown in Figures 2*c* and *d*, iv) reproduced the experimental total and partial atomic PDF data in very good detail. As such, within the limits of experimental accuracy, RMC-refined 3D atomic models shown in Figure 3*a* can be considered as the most likely, ensemble-averaged 3D atomic structures of pure Pt and Fe@Pt NCs, and so are fit for their purpose [25-27]. That is, 3D positions of atoms in the structures can be used to assess the atomic structure-function relationship for the respective NC samples.

The catalytic functionality of Fe@Pt NCs for ORR was determined by the rotating disk electrode technique in 0.1 M $HClO_4$ electrolyte at room temperature, as described in the Methods section of SI. For reference, without loss of generality, ORR over catalyst surface can be expressed as $O_2 + 4H^+ + 4e^- \rightarrow H_2O$, that is, oxygen molecules adsorbed and reduced at the surface react with protons supplied to the surface to form water. Tafel plots of the specific activity of Fe@Pt NCs for ORR are summarized in Figure S2. The plots clearly show that the ORR kinetics of Fe@Pt NCs is superior to that of standard Pt NCs in the high potential range (0.88 V - 0.98 V). In particular, the mass activity (MA) for ORR, which is relevant to practical applications, increases in the order pure Pt < Fe@2Pt < Fe@1.5Pt < Fe@1Pt NCs. The improvement in the MA of Fe@Pt NCs for ORR is best illustrated in Figure 3*d*. Qualitatively, it has been attributed to one or more of the following factors: i) ligand/electronic effects arising from charge exchange between atoms at the Fe core@Pt skin interface, ii) strain effects arising from the difference between the size of atoms forming the NC core and skin and iii) geometric effects where a particular configuring of atoms from Pt skin are beneficial to ORR [4, 13]. Here we show that, though counterintuitive, it is proportionate to the increase in the effective coordination number of atoms from Pt skin with the decrease in its thickness.

Magnetic characteristics of Fe@Pt NCs were determined on a SQUID magnetometer from Quantum Design. Hysteresis curves for Fe@Pt NCs measured at 2 K are shown in Figure S3.

Coercivity, H_c, values for Fe@1Pt, Fe@1.5Pt and Fe@2Pt NCs determined from the curves are 2120 Oe, 2080 Oe and 2050 Oe, respectively. Zero field and field (100 Oe) cooled magnetization curves for Fe@Pt NCs are shown in Figure 4*a*. The curves exhibit a clear "blocking effect", where the magnetic moment of Fe cores is pinned to a direction of easy magnetization. The effect is the hallmark of superparamagnetism [28]. The so-called "blocking temperature", T_B, for Fe@1Pt, Fe@1.5Pt and Fe@2Pt NCs was determined from the "cusp" in the magnetization measured in the absence of magnetic field. Values turned out to be 15 K, 11 K and 8 K, respectively. According to theory of superparamagnetic clusters, H_c may not depend on the cluster's size significantly whereas T_B is expected to decrease fast with the cluster's size, so long the latter is < 6 nm [28, 29]. Indeed, this is what we observe. On grounds discussed in the Methods section of SI (see *eq. S5* and related to it text) and using the experimental data for T_B, the effective magnetic anisotropy for Fe@1Pt, Fe@1.5Pt and Fe@2Pt NCs was estimated to be in the order of 9.2×10^5 J/m^3, 9.09×10^5 J/m^3 and 9.04×10^5 J/m^3, respectively. The values are considerably larger than the intrinsic anisotropy for bulk bcc Fe (4.8×10^4 J/m^3). Considering the polyhedral shape of Fe cores (see Figure 4b) and the fact that Fe@Pt NCs are well separated from each other (see Figures 1 and S1), i.e. unlikely to experience dipole-dipole type magnetic interactions, the observed large anisotropy values can be attributed to the abrupt change in the atomic coordination and broken 3D periodicity at the core's surface, including core's surface relaxation effects [28-30]. Here is to be added that the total magnetic moment of Fe clusters is composed from the magnetic moments of the constituent atoms and so can be many tens of μ_B, if not larger [28-30]. The contribution of surface atoms to the moment and anisotropy of Fe clusters and the evolution of the moment with the cluster's size though is not well understood. Here we show that the missing knowledge can be provided by *3d*-band model theory based on ensemble-averaged positions of atoms forming actual Fe clusters.

The ORR activity and superparamagnetism of Fe@Pt NCs can be rationalized by summarizing the general features of the valence electron structure of constituent Fe and Pt atoms. In particular, the valence electron configuration of single Pt atom is $5d^9 6s^1$. However, at the bulk scale, a small number of *5d*-electrons are pushed into higher-energy *6s* and *6p* states through a process known as *(sp)−d* hybridization, giving rise to the so-called *5d*-holes. Hence, the actual valence electron configuration of bulk Pt is $5d^{8.66} 6(sp)^{1.34}$. Studies have found that the ORR activity of Pt surfaces is influenced strongly by the degree of *(sp)−d* hybridization, width,

and energy position of surface *5d*-electron band, and occupied surface *5d*-electron density of states (*d*-DOS) [4, 31-33]. On the other hand, when Fe atoms ($3d^6 4s^2$) are brought together to form a solid, the valence *3d*-electrons of Fe are distributed over the so-called majority (*3d*↑ spin-up) and minority (*3d*↓ spin-down) bands whereas valence *4s*-electrons occupy a nearly half-empty *4(sp)*-band. The majority and minority *d*-bands intersect the Fermi level and, due to strong (*dd)* and *(sd)* hybridization effects leading to the so-called *3d*-holes, the magnetic moment of Fe atoms appears 2.2 μ_B, instead of the expected from the Hund's rules 3μ_B. For Fe clusters, this picture changes significantly because a large fraction of the atoms are on the surface and so have a reduced number of nearest neighbors. Accordingly, the *3d*-electrons of surface Fe atoms are less delocalized, i.e. the width of both *3d*↑ and *3d*↓ bands diminishes. Besides, the energy position of *3d*↑ and *3d*↓ bands for Fe surface atoms shift with respect to the Fermi level and so the number of *3d*-holes in the *3d*↑ band is reduced. Ultimately, the magnetic moment of surface atoms in Fe clusters approaches 3 μ_B. [29, 34, 35].

As discussed in the Methods section of SI (see *eqs. S27, S28 and S29*), the width, energy position and occupancy of valence *d*-bands (*d*-DOS), i.e. the valence *d*-band structure, in the vicinity of atomic sites on the surface of transition (Fe) and noble (Pt) metals are largely determined by the local coordination of the atoms. Therefore, we used the so-called effective coordination numbers, CN_{eff}, to directly assess the atomic structure-function relationship for Fe@Pt NCs, where function pertains to applications in the areas of superparamagnetism and ORR catalysis. The CN_{eff} were computed from the 3D positions of atoms in the RMC-refined structures of Fe@Pt NCs using eq. *S30*. Here is to be underlined that the approach of using CN_{eff} instead of the traditional counting of near neighbors is similar to the embedded-atom method, where the valence electron density at an atomic site is approximated by a superposition of valence electron densities of nearby atoms which, in turn, are a superposition of the valence electron density of the first neighbors of each of those atoms. Besides, CN_{eff} have already proven useful in describing the ORR activity of Pt surfaces and magnetic properties of Fe [37-40]. In computing CN_{eff} for Pt atoms we used the first physical minimum in the atomic PDF for pure Pt NCs at 3.2 Å as a maximum near-neighbor distance. Also, the CN_{eff} were normalized against the maximum possible number of near neighbors for Pt atoms occupying a close packed $(111)_{fcc}$ monolayer, that is 6. In computing CN_{eff} for Fe atoms we used the first physical minimum in the Fe-Fe partial PDFs at 3.1 Å as a maximum near neighbor distance. Also, CN_{eff} were normalized

against the total number of near and next near neighbors for Fe atoms in bulk bcc Fe, that is 14 (8+6; see Figure 2b). The choice was appropriate because, as the broad nature of the first peak in the experimental Fe-Fe partial PDFs shows (see Figure 2d), bcc Fe cores are significantly relaxed at atomic level and so the partitioning of the coordination environment of atoms forming the cores into near and next-near neighbors is indeed hardly possible. The so-obtained CN_{eff} for top surface Pt atoms in Fe@Pt NCs are summarized in Figure 3*d*. The CN_{eff} for Fe atoms in Fe@Pt NCs are summarized in Figure 4*c*. Distribution of near-neighbor (bonding) distances for top surface Pt atoms was also computed and normalized in terms of strain using the Pt-Pt pair distance in bulk Pt, which is 2.775 Å, as a reference value. The distribution is shown in Figure 3*b*.

As data in Figure 3*b* show, Pt atoms forming the "skin" of Fe@1Pt NCs are considerably compressed (~1.2 % on average), i.e. have come considerably closer together, as compared to top surface atoms in pure Pt NCs. On average, top surface Pt atoms in Fe@1.5Pt and Fe@2Pt NCs also appear considerably compressed, though to a lesser extent. On the other hand, on average, top surface atoms in pure Pt NCs are hardly compressed as compared to atoms on a perfect (111) facet of bulk Pt. We argue that the observed compressive strain of Pt skin in Fe@Pt NCs is due to i) the lack of structural coherence at the bcc Fe@fcc Pt interface and ii) mismatch between the size of Fe and Pt atoms forming the NC core and skin, respectively. Experimental studies have shown and theory predicted that Pt surfaces compressed by 1 % to 2 % function as ORR catalysts better than unstrained Pt surfaces [1, 4, 31, 41]. Hence, the observed here change in the surface strain in Fe@Pt NCs with the thickness of Pt skin, that is ~ 0.2 %, 0.8 %, 1 % and 1.2 % surface strain for pure Pt, Fe@2Pt, Fe@1.5Pt and Fe@1Pt NCs, respectively, may well explain the observed trend in their ORR activity. Furthermore, effectively, the decrease in surface Pt-Pt bonding distances in Fe@Pt NCs leads to an increase in the average surface CN_{eff} . In particular, the number of top surface Pt atoms with CN_{eff} = 5 and 6 is about 54 %, 41%, 34 % and 15 % for Fe@1Pt, Fe@1.5Pt and Fe@2Pt and pure Pt NCs, respectively. As exemplified in Figure 3*c*, the relative increase in the CN_{eff} is most pronounced for atoms near edges of Pt skin whereas atoms at the edges largely remain under-coordinated, that is, 3- and 4-fold coordinated. According to the *d*-band center theory, bond order conservation arguments and experimental observations [4, 31, 41, 42], higher coordinated sites on Pt surfaces are less reactive than low coordinated ones, in particular with respect to oxygen species, and so are likely to accelerate ORR kinetics.

Remarkably, as data in Figure 3*d* show, when normalized against the total number of Pt atoms in the respective NCs, the percentage of increase in the CN_{eff} for Fe@Pt NCs with the decrease in the thickness of Pt skin matches the respective enhancement factor in ORR activity. The observation underlines the importance of incommensurate guest-host nanostructures, such as NCs comprising a Fe cluster-like core nested inside a super-thin Pt skin, and relatively longer-range surface coordination effects, as reflected in CN_{eff}, in tuning up the functionality of Pt-based ORR catalysts. Also, it is a prime example of not only revealing but also quantifying the structure-catalytic functionality relationship for metallic NCs on the basis of ensemble-averaged 3D positions of atoms in the NCs, and not just establishing trends [4, 42].

Using a streamlined *3d*-band model for the magnetic properties of Fe clusters (see *eq. S6*) and CN_{eff} in Figure 4*c*, we computed the magnetic moment, μ, for each atom in the cores of Fe@Pt NCs, the average magnetic moment per atom, $<\mu_R>$, as a function of the radial distance, *R*, from the center of the cores and the average magnetic moment per atom, $<\mu_N>$, for each of the cores [37, 38]. In the computations we used the experimental values for the magnetic moment of Fe atoms in bulk, $\mu_{Fe\ (bulk)} = 2.22\ \mu_B$ and Fe-Fe dimers, μ_{Fe} (dimer) = $3.25\ \mu_B$ [34, 35]. 3D rendition of Fe cores in Fe@Pt NCs where each constituent atom is assigned a magnetic moment computed as described above is shown in Figure 4*b*. The evolution of $<\mu_R>$ with *R* is shown in Figure 4*c*. As can be seen in the Figure, atoms at the very center of Fe cores have CN_{eff}=14 and so carry the magnetic moment of bulk Fe atoms. Also, due to the gradual decrease in the respective CN_{eff}, the closer Fe atoms to the core surface the higher their magnetic moment. Notably, the magnetic moment of near-surface Fe atoms with a $CN_{eff} < 6$ approaches $3\ \mu_B$ which corresponds to a valence electron structure of the $5(3d\uparrow)2(3d\downarrow)1(4s)$-type.

Values for $<\mu_N>$ are also shown in Figure 4*c* together with relevant experimental data, $<\mu_N^{exp}>$, resulted from "Stern-Gerlach" type studies [43, 44]. As can be seen in the Figure, $<\mu_N>$and $<\mu_N^{exp}>$ agree reasonably well. Considering that each $<\mu_N^{exp}>$ data point appears as an average of the magnetic moments of a large assembly of Fe clusters each comprising N atoms (e.g. see *eq. S33* and related to it text in SI), the observed agreement indeed may not come as a surprise. Within the limits of a spherical cluster model (see eq. *S31*), it may be conjectured that $<\mu_N>$ would evolve as $N^{-1/3}$. As can be seen in Figure 4*c* though, the convergence of $<\mu_N^{exp}>$ to the bulk value with increasing N is much faster. Evidently, this model is too simple to account

for the observed cluster-size dependence of $<\mu_N>$. Other models assuming that Fe clusters with a particular number of atoms, N, would appear as a particular canonical polyhedron such as, for example, icosahedron for N < 100, rhombic dodecahedron for 100 < N < 500 and cuboctahedron for N > 500 [45, 46], fail in describing reasonably well the observed functional dependence of $<\mu_N^{exp}>$ on N either [38]. We argue that, largely, the failure is due to ignoring the ensemble-average nature of $<\mu_N^{exp}>$ [35, 47, 48]. Indeed, due to intrinsic surface relaxation effects and lack of 3D periodicity, clusters comprising N atoms may appear as an assembly of similar but not necessarily the same polyhedral structures [49-52] and so are likely to carry similar but not the same magnetic moments. As evidenced by data in Figure 4*c*, the cluster-size dependence of both $<\mu_N^{exp}>$ obtained elsewhere and $<\mu_N>$ obtained here may well be described by a sigmoid-type function related to the Langevin function used to describe the dependence of the large magnetic moment of transition metal clusters on the applied external magnetic field and temperature (see *eqs. S32-S34*). That is, when the ensemble-average nature of $<\mu_N^{exp}>$ data resulted from "Stern-Gerlach" type experiments and $<\mu_N>$ derived from ensemble-averaged 3D atomic structure data is accounted for properly, not only the latter appear a true representation of the former but also the cluster-size (N) dependence of both quantities can be described by statistical theory for non-interacting superparamagnetic clusters. This is a prime example of determining a fundamental relationship between the atomic-scale structure and functional properties of composite metallic NCs, in particular superparamagnetic properties, on the basis of ensemble-averaged 3D positions of atoms constituting a nested component of the NCs.

Fluctuations in the chemistry, size and shape of nanosized materials produced and used en masse, such as metallic NCs, can be significant and are hard to avoid. Besides, due to their cluster-bulk solid duality, NCs with the same size (N) and overall chemical composition may appear, including kinetically trapped, as various virtually isostructural polymorphs (e.g. somewhat differing in the degree of local structural disorder alone) from a pool of energetically favorable structures, often referred to as a "structural landscape" [50, 53]. Nevertheless, as demonstrated here, characteristic structural features and physicochemical properties of NCs produced with due care in pursuit of given functionality appear as durable macroscopic quantities. Indeed this is the reason behind the consistency of NC's functionality in practical applications. The quantities are an average over the usually immense ensemble of NCs required by the applications and can be measured with high precision. In particular, the experimental

approach employed here allows determining ensemble-averaged 3D positions of atoms in structurally complex, multi-functional NCs. The knowledge helps not only understand but also quantify the structure-function relationship for the studied ensembles, thereby enabling a rational design approach to producing better NCs.

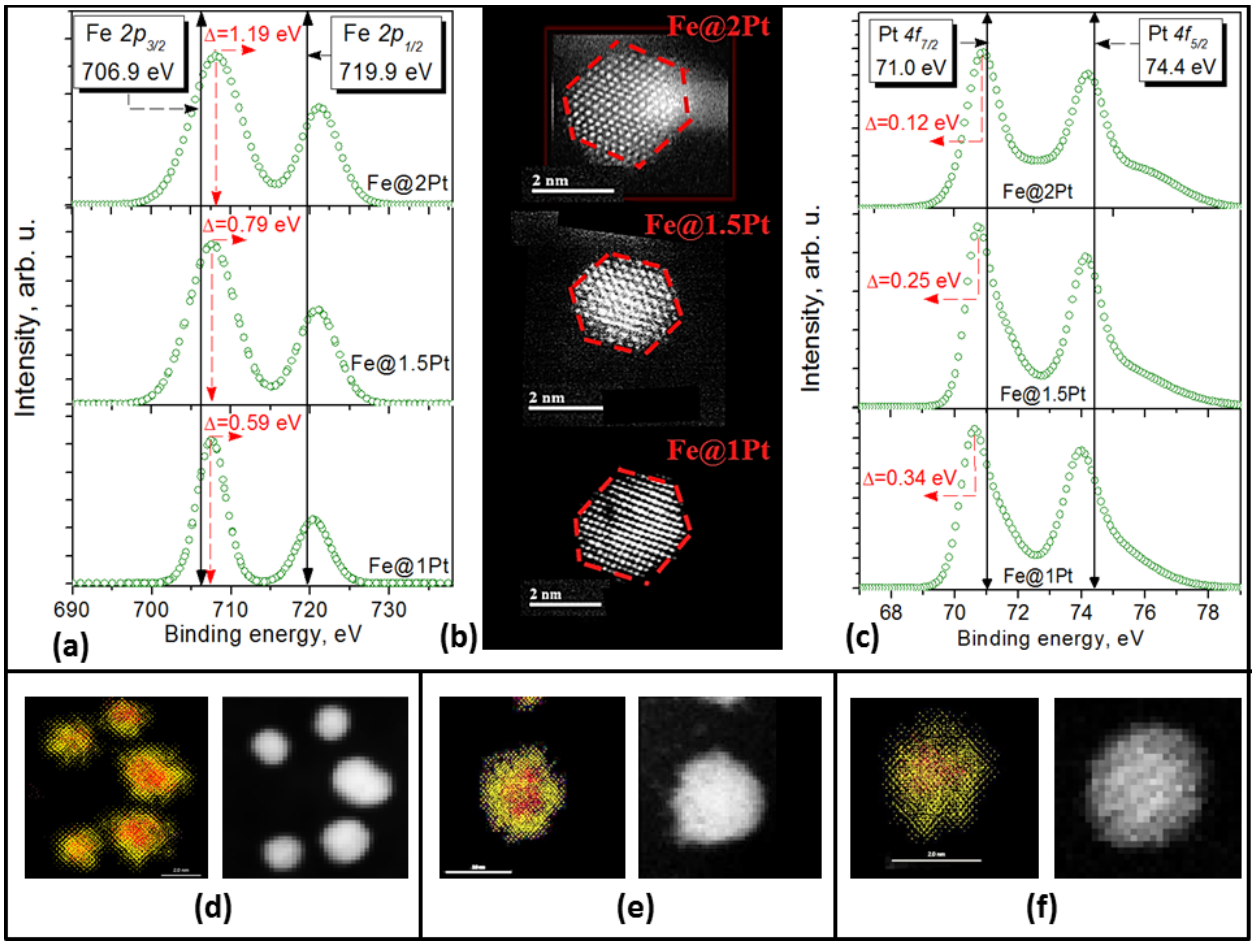

Figure 1. ***(upper panel)*** (a) Typical XPS Fe $2p_{3/2}$ and $2p_{1/2}$ spectra for Fe@Pt NCs. The positive shift, Δ, of the binding energy of Fe atoms in the respective NCs (red broken lines) is evaluated with respect to the Fe $2p_{3/2}$ spectral line (black solid line) characteristic to bulk Fe. (b) Representative HAADF-STEM images of Fe@Pt NCs. Images indicate that the NCs are with an average size of approximately 2.5(± 0.3) nm and polyhedral shape. Red broken lines outline the well-defined facets of the NCs. (c) Typical XPS Pt $4f_{7/2}$ and $4f_{5/2}$ spectra for Fe@Pt shell NCs. The negative shift, Δ, of the binding energy of Pt atoms in the respective NCs (red broken lines) is evaluated with respect to the Pt $4f_{7/2}$ spectral line (black solid line) characteristic to bulk Pt. ***(lower panel)*** Representative EDS elemental maps and HAADF-STEM images of (d) Fe@1Pt, (e) Fe@1.5Pt and (f) Fe@2Pt NCs. Fe atoms are in red and Pt atoms are in yellow.

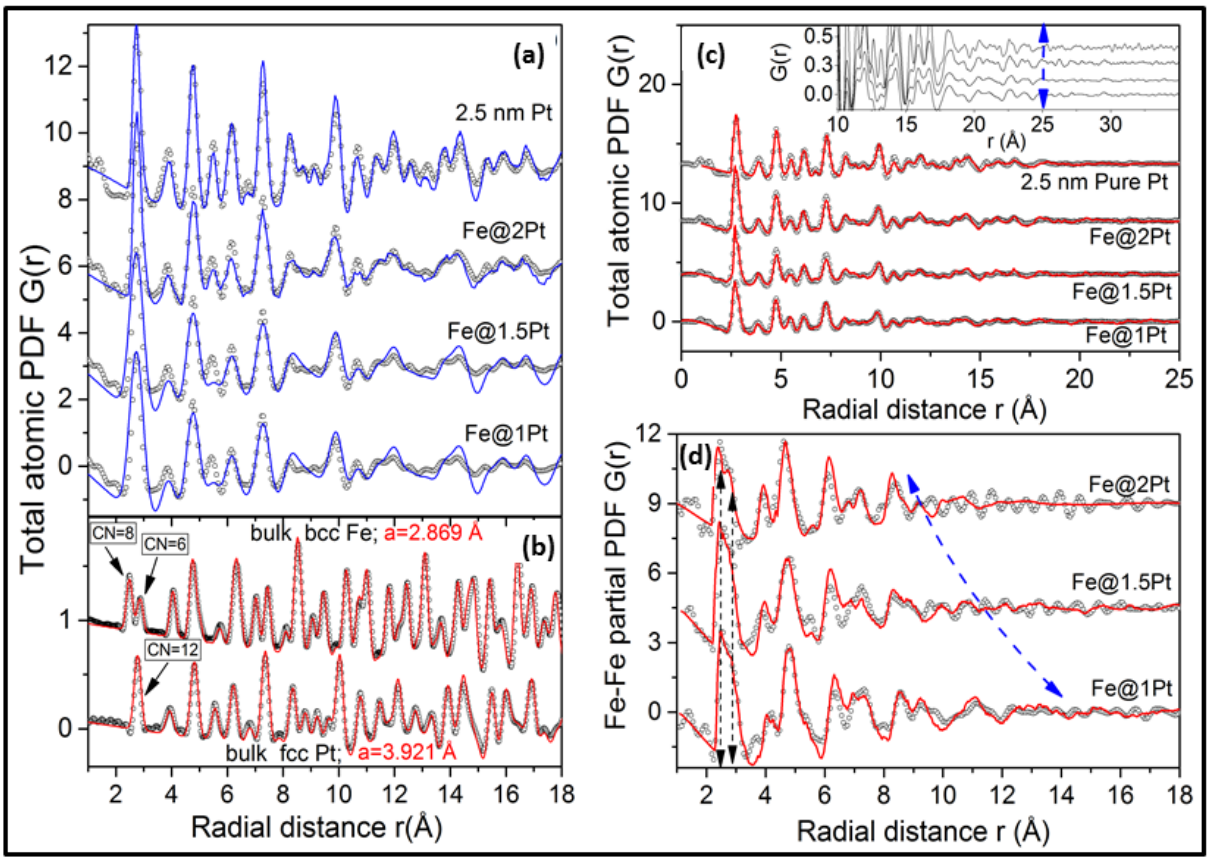

Figure 2. ***(left)*** (a) Experimental (symbols) and computed (blue line) atomic PDFs for pure 2.5 nm Pt and Fe@Pt Ncs. The computed PDFs are derived from MD optimized models featuring the NCs as close packed atomic layers stacked in an fcc-type sequence. (b) Experimental (symbols) and computed (red line) atomic PDFs for bulk bcc Fe and fcc Pt. The computed PDFs are based on an infinite bcc- and fcc-type lattice with a parameter a=2.869 and a=3.921 Å, respectively. Arrows emphasize the difference between near-neighbor coordination spheres in bcc- (8+6 near neighbors) and fcc-type (12 near neighbors) metals. ***(right)*** (c) RMC fits (red lines) to the experimental (symbols) total atomic PDFs for 2.5 nm Pt and Fe@Pt NCs. The higher-r part of the experimental data is shown in the inset. Vertical broken line (in blue) marks the real-space distance at which the physical oscillations in the PDF data decay to zero. (d) RMC fits (red line) to the experimental (symbols) Fe-Fe partial PDFs for Fe@Pt NCs. Inclined broken line (in blue) emphasizes the increasing length of structural coherence in the Fe cores with the diminishing thickness of Pt skin. Vertical broken lines (in black) show the nearly merged first and a bit more distant second coordination spheres of Fe atoms in the cores. The RMC fits in (c) and (d) reflect the atomic structures shown in Figure 3a. The quality factors R_w, for the structures are in the order of 7 (± 3) %.

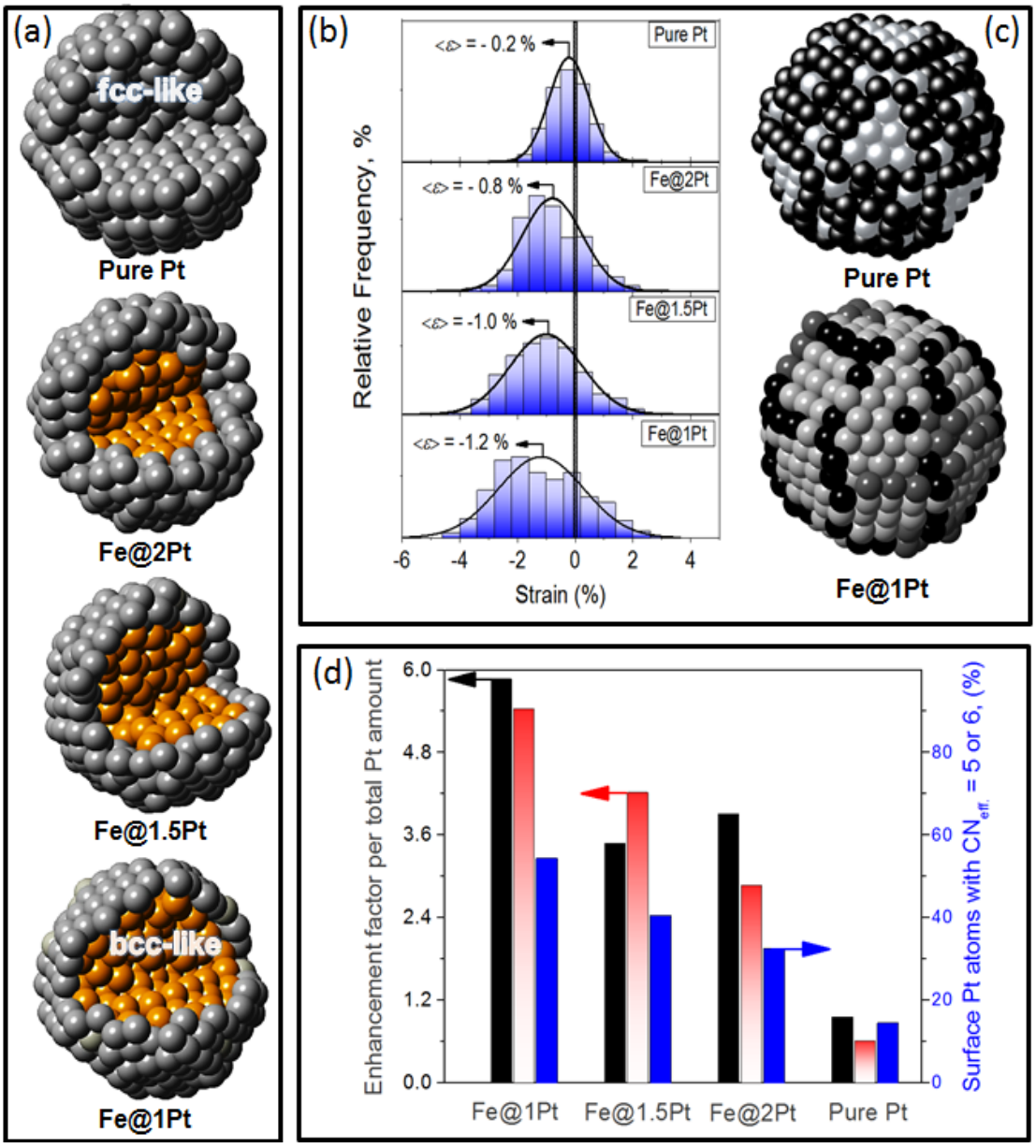

Figure 3. ***(a)*** Full-scale structures for 2.5 nm fcc Pt and bcc Fe@fcc Pt NCs determined as described in the text. Pt atoms are in gray and Fe atoms are in light brown. ***(b)*** Distribution of bonding distances between surface Pt atoms from the structures shown in ***(a)***. The distances appear "compressed" (in %) when normalized against the bulk Pt-Pt bonding distance of 2.775 Å as a reference point. ***(c)*** Effective coordination of surface sites in pure 2.5 nm Pt and Fe@1Pt NCs as derived from the respective structures shown in ***(a)***. Surface Pt atoms with an effective 1st CN=5 or 6 and smaller than 5 are given in gray and black, respectively. ***(d)*** Percentage of surface atoms in 2.5 nm pure Pt and Fe@Pt NCs with an effective 1st CN=5 or 6 (blue bars). Enhancement (red bars) of the catalytic activity of Fe@Pt NCs for ORR (vs pure Pt NCs) as predicted from the percentage of surface Pt atoms with an effective 1st CN=5 or 6 (vs 1st CN smaller than 5). Enhancement (black bars) of the (mass) catalytic activity of Fe@Pt NCs for ORR (vs pure 2.5 nm Pt particles) obtained by CV and RDE experiments described in the Methods Section of SI.

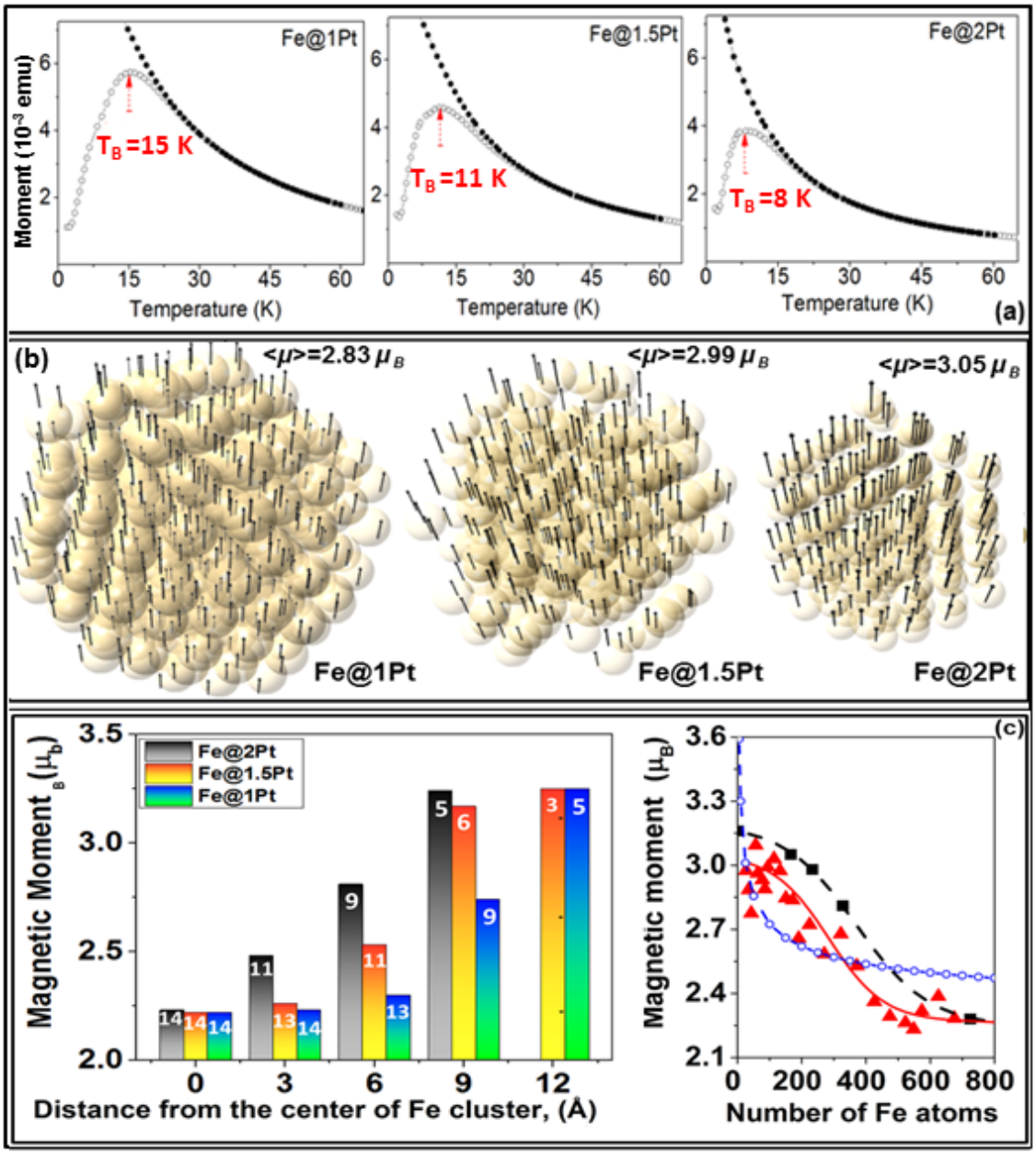

Figure 4. ***(a)*** Temperature dependence of the zero field cooled (open circles) and field (100 Oe) cooled (filled circles) magnetization for Fe@Pt NCs. The blocking temperature, T_B, is given for each data set. ***(b)*** Atoms (circles) forming Fe cores of Fe@Pt NCs. Arrows represent the magnetic moments of individual atoms assessed as explained in the text for $T<T_B$. The average magnetic moment per atom, $\langle\mu\rangle$, in the respective cores for $T < T_B$ and the size of cores, *d*, are also given. ***(c)*** (left) $\langle\mu\rangle$ (bars) and CN_{eff} (numbers inside the respective bars) as a function of the distance from the center of Fe cores. (right) Experimental (red triangles), 3D structure computed (black rectangles) and empirical ($\sim N^{-1/3}$; blue circles) $\langle\mu_N\rangle$ as a function of the core size. Solid line in red and broken line in black are sigmoidal fits to the respective data sets. Blue line is a guide to the eye.

AUTHORS INFORMATION

Corresponding Author
* E-mail: free to petko1vg@cmich.edu

Notes
The authors declare no competing financial interest.

ACKNOWLEDGMENTS

This work was supported by DOE-BES Grant DE-SC0006877 and the National Research Foundation of Korea under grant NRF-2016R1A2B4014012. The work also used resources of the Advanced Photon Source at the Argonne National Laboratory provided by the DOE Office of Science under Contract No. DE-AC02-06CH11357.

REFERENCES

1. M. Shao, Q. Chang, J.-P. Dodelet and R. Chenitz *Chem. Rev*. 116 (2016) 3594.
2. X. Xu, Sh. Yin, R. Moro and W. A. de Heer *Phys. Rev*. **B 78** (2009) 054430.
3. Q. A. Pankhurst, J. Connolly, S. K. Jones and J. Dobson J. Phys. D: Appl. Phys. **36** (2003) R167.
4. B. Hammer and J. K. Norskov *Adv. Catal*. **45** (2007) 71.
5. R. Ferrando, J. Jellinek and R. L. Johnston, *Chem. Rev*. **108** (2008) 845.
6. I. Robinson and R. Harder *Nat. Mat*. **8** (2009) 291.
7. Y. Yang, Ch.Chun Chen, M C. Scott, C. Ophus, R. Xu, A. P. Jr., L. Wu, F. Sun, W. Theis, J. Zhou, M. Eisenbach, P. R. C. Kent, R. F. Sabirianov, H. Zeng, P. Ercius and J. Miao Nature 542 (2017) 75.
8. J. Miao, P. Ercius and S. J. L. Billinge *Science* **353** (2016) 1380.
9. V. Petkov. *Mater. Today* **11** (2008) 28.
10. C. G. Hadjipanayis, M. J. Bonder, S. Balakrishnan, X. Wang, X.H. I. Mao, G. C. Hadjipanayis *Small* **4 (2008)** 1925.
11. J. Ticek, Z. Sofer, D. Bousa, M. Pumera, K. Hola, A. Mala, K. Polakova, M. Navrodova, K. Cepe, O. Tomanec and R. Zboril *Nat. Comm*. (2016) 7:12879.
12. M. K. Debe, *Nature* **486** (2012) 43.
13. J.-H. Jang, E. Lee, J. Park, G. Kim, S. Hong and Y.-U. Kwon *Sci. Rep.* **3:2872** (2013).
14. H. P. Erickson, *Biol. Proc. Online* **11** (2009) 32.
15. M. Xue and Q. Guo *Chem. Phys. Lett.* **551** (2012) 92.
16. T. Toda, H. Igarashi, H. Ucida and M. Watanabe *J. Electrochem. Soc.* **146** (1999) 3750.
17. B. R. Cuenya, J. R. Croy, L. K. Ono, A. Naitabi, H. Heinrich, W. Keune, J. Zhao W.
18. Sturhahan, E. E. Alp and M. Hu *Phys. Rev. B* **80** (2009) 125412.
19. Z. Bayindir, P.N. Duchesne, S. C. Cook, M. A. MacDonald and P. Zhang *J. Chem. Phys.* **131** (2009) 244716.
20. R. Cerny and V. Favre-Nicolin, *Z. Kristallogr*. **222** (2007) 105.
21. Y. Waseda in "*Anomalous X-Ray Scattering for Materials Characterization: Atomic-*

Scale Structure Determination"; (Springer: Berlin, 2002).
22. T. C. Monson, E. L. Venturini, V. Petkov, Y. Ren, M. Judith and D.L. Huber *J. Magn. Mag. Mater.* **331** (2013) 156.
23. S. Grazulis, D. Chateigner, R. T. Downs, A. F. T. Yokochi, M. Quiros, L. Lutterotti, E. Manakova, J. Butkus, P. Moeck and A.Le Bail *J. Appl. Cryst*. **42** (2009) 726; http://www.crystallography.net/cod/
24. Pearson, W. B. in "*The crystal chemistry and physics of metals and alloys"* (New York: Wiley-INTERSCIENCE, **1972**).
25. V. Petkov, B. Prasai, Y. Ren, S. Shan, J. Luo, P. Joseph and C.-J. Zhong *Nanoscale* **26** (2014) 10048.
26. B. H. Toby and T. Egami *Acta Cryst. A*, **48** (1992) 336.
27. B. E. Warren, in "*X-ray Diffraction*" (Addison-Wesley Publ. Co; **1969**).
28. J. M. D. Coey, Magnetism and Magnetic Materials (Cambridge University Press, Cambridge, 2010).
29. D. L. Leslie-Pellecky and R. D. Rieke *Chem. Mat*. **8** (1996) 1770.
30. S. Oyarzu, A. Tamion, F. Tournus, V. Dupuis and M. Hillenkamp, *Sci. Rep*. (2015) 5:14749.
31. V. Stamenkovic, B. S. Mun, M. Arenz, K. J. J. Mayrhofer, C. A. Lucas, G. Wang, P.N. Ross and N. M. Markovic *Nat. Mat*. **6** (2007) 241.
32. J. K. Norskov, J. Rossmeisl, A. Logadottir, L. Lundkvist, J. R. Kitchin, T. Bligaard and H. Jonsson *Phys. Chem*. B ***108*** (2004) 17886.
33. V. Stamenkovic, B. S. Mun, K. J. J. Mayrhofer, P. N. Ross, M. N. Markovic, J. Rossmeisl, J. Greeley and J. K. Nørskov, *Angew. Chem. Int. Ed*. **45** (2006) 2897.
34. D. J. Sellmyer and R. Skomski (Eds.) in "*Advanced Magnetic nanostructures*" (Springer; 2005).
35. H. Kronmüller and S. Parkin (Eds.) in "*Handbook of Magnetism and Advanced Magnetic Materials"* Vol. 3. (Wiley; 2007).
36. O. Sipr, M. Kosuth and H. Ebert *Phys. Rev. B* **70** (2004) 174423.
37. D. Tomanek , S. Mukherjee and K. H. Bennemann *Phys. Rev. B* **28** (1983) 665.
38. J. Zhao, X. Chen, Q. Sun, F. Liu and G. Wang *Phys. Lett. A* **205** (1995) 308.
39. X. Ma and H. Xin, *Phys. Rev. Lett*. **118** (2017) 036101-1.
40. F. Calle-Vallejo, J. Tymoczko, V. Colie, Q. H. Vu, M. D. Pohl, K. Morgenstern, D. Loffreda, Ph. Sautet, W. Schuhmann and A. S. Bandaenka *Science* **350** (2015) 185.
41. J. X. Wang, H. Inada, L. Wu, Y. Zhu, Y. Choi, P. liu, W.-P. Zhou and R. Adzic *J. Am. Chem. Soc.* **131** (2009) 17298.
42. B. C. Han, C. R. Miranda and G. Ceder *Phys. Rev. B* **77** (2008) 075410.
43. I. M. L. Billas, J. A. Becker, A. Chatelain and W. A. de Heer *Phys. Rev. Lett*. **71** (1993) 4067.
44. I. M.L. Billas, A. Chatelain and W. A. de Heer *Science* **265** (1994) 1682.
45. N. A. Besley, R. L. Johnson, A. J. Stace and J. Uppenbrink *J. Mol. Str. (Theochem)* **341** (1995) 75.
46. Largely, the vertices of canonical polyhedra are positioned in space to satisfy the following properties: i) all the edges are tangent to a unit sphere, ii) the origin is the center of gravity of the points at which the edges touch the unit sphere and iii) the faces are flat. Here, the unit sphere of a canonical polyhedron is a sphere which is tangent to every edge of the polyhedron, i.e. touches it at a single point. Note that Archimedean solids, Bernals and

Kaspers polyhedra widely used in studies of the atomic structure of bulk materials are canonical polyhedra.
47. X. Xu, S. in. R. Moro and W. A. de Heer, *Phys. Rev. B 78* (2008) 054430.
48. Y. Xie and J. A. Blackman *J. Phys.: Condens. Matter* **15** (2003) L615.
49. J. Uppenbrink and D. J. Wales, *J. Chem. Phys*. **96** (1992) 8520.
50. Z. Y. Li, N. P. Young, M. Di Vece, S. Palomba, R. E. Palmer, A. L. Bleloch, B. C. Curley, R. L. Johnston, J. Jiang and J. Yuan *Nature* **451** (2008) 46.
51. R. I. Robinson *Nat. Mat*. **7** (2008) 275.
52. A. D. Bruce and R. A. Cowley *J. Phys. C: Solid State Phys*. **11** (1978) 3609.
53. G. R. Desiraju, *Crys. Growth & Desig.* **8** (2008) 4031.

Supplementary Information

Ensemble averaged structure-function relationship for composite nanocrystals: magnetic bcc Fe clusters with catalytically active fcc Pt skin

Valeri Petkov,[1] Binay Prasai,[1] Sarvjit Shastri,[2] Hyun-Uk Park,[3] Young-Uk Kwon [3] and Vassil Skumryev [4]

[1]Department of Physics, Central Michigan University, Mt. Pleasant, Michigan 48859, United States
[2]X-ray Science Division, Advanced Photon Source, Argonne National Laboratory, Argonne, Illinois 60439, United States
[3]Department of Chemistry, Sungkyunkwan University, Suwan 16419, Republic of Korea
[4]Department of Physics, Universitat Autònoma de Barcelona, Bellateria 08913, Spain

Methods:

i) Synthesis of composite Fe core-Pt skin NCs

The Fe core-Pt skin nanocrystals (NCs) were synthesized by one step ultrasound-assisted polyol reactions between Fe(III) acetylacetonate, $Fe(C_5H_7O_2)_3$, and Pt(II) acetylacetonate, $Pt(C_5H_7O_2)_2$. In particular, mixtures of $Fe(C_5H_7O_2)_3$ and $Pt(C_5H_7O_2)_2$ in pre-desired ratios were sonicated in ethylene glycol in the presence of fine carbon powder (Ketjen black), filtered, washed and then dried under vacuum. The mixtures wherein the ratio of $Fe(C_5H_7O_2)_3$ to $Pt(C_5H_7O_2)_2$ was as small as 0.1 yielded NCs with a relatively larger Fe core, that is approximately 330 atoms, and Pt skin as thin as one atomic layer. The mixtures wherein the ratio of $Fe(C_5H_7O_2)_3$ to $Pt(C_5H_7O_2)_2$ was as large as 1.2 yielded NCs with a relatively small Fe core, that is approximately 160 atoms, and Pt skin comprising two atomic layers. Three samples of Fe core-Pt shell NCs were synthesized with the size of Fe core and the thickness of Pt skin were fine-tuned through varying the $Fe(C_5H_7O_2)_3$ to $Pt(C_5H_7O_2)_2$ ratio so that the overall size of resultant NCs was kept constant and close to 2.5 nm. More details of the synthesis protocol can be found in ref. [S1].

ii) Determining the overall chemical composition, size, shape and chemical pattern of composite Fe core-Pt skin NCs

The overall (bulk) chemical composition of the three Fe core-Pt skin samples studied here was determined by inductively coupled plasma atomic emission spectroscopy (ICP-AES). Measurements were done on a Perkin Elmer 2000 DV ICP-AES instrument. Calibration was done against standards dissolved in the same acid matrix as the unknowns. Several batches of the unknowns were analysed thus ensuring < 2 % error in the overall chemical composition. Experimental data showed that the overall chemical composition of Fe core-Pt skin samples is very close to the loading ratios of $Fe(C_5H_7O_2)_3$ and $Pt(C_5H_7O_2)_2$ precursors, that is, $Fe_{0.4}Pt$ ($Fe_{166}Pt_{421}$), $Fe_{0.7}Pt$ ($Fe_{244}Pt_{351}$) and $Fe_{1.2}Pt$ ($Fe_{363}Pt_{297}$).

The size, shape and chemical pattern of Fe_xPt (x=0.4. 07 and 1.2) NCs and standard Pt NCs were determined by High-Angle Annular Dark-Field (HAADF) Scanning TEM (STEM) experiments done on a JEOL JEM 2100F instrument equipped with a CEOS hexapole probe. The

instrument was operated at 200 keV in STEM mode. The lens settings combined with the corrector tuning gave a spatial resolution of ~ 90 pm. Exemplary HAADF-STEM images are shown in Figure S1. HAADF-STEM images of selected Fe_xPt (x=0.4, 0.7 and 1.2) NCs are shown in Figure 1(***b***). As can be seen in the Figures, Fe_xPt (x=0.4. 07 and 1.2) and pure Pt NCs are rather uniform in terms of size and shape. To be more specific, the NCs appear with an average size of 2.5 (± 0.2) nm, polyhedral shape and well-defined facets. Furthermore, the NCs possess a good degree of crystallinity as evidenced by the lattice fringes in the respective images.

EDS maps of Fe_xPt (x=0.4. 07 and 1.2) NCs are shown in Figure 1(d, e and f).The maps indicate that the NCs have a core-skin morphology. To evaluate the number of surface Pt layers on top of Fe cores, we carried out simplistic calculations using the experimental ICP-AES data for the chemical composition of the NCs, HAADF-STEM data for the size of the NCs (~2.5 nm) and well-known size of Fe (2.52) Å and Pt (2.775 Å) atoms [S2]. In particular, for $Fe_{1.2}Pt$ NCs we found that Pt skin, that is the difference between the radius of the NCs and the radius of Fe core, is approximately 1 monolayer thick. For $Fe_{0.7}Pt$ and $Fe_{0.4}Pt$ NCs the skin turned out to be about 1.5 and 2 Pt layers thick, respectively. The so-obtained independent estimate of Pt skin thicknesses matched well the pre-desired number of Pt layers. Hence, hereafter, Fe_xPt (x=0.4. 07 and 1.2) NCs are referred to as Fe@1Pt, Fe@1.5Pt and Fe@2Pt NCs, respectively.

iii) X-ray photoelectron spectroscopy (XPS) studies on Fe core-Pt skin NCs

The electronic properties of Fe and Pt atoms forming the core and skin of Fe@1Pt, Fe@1.5Pt and Fe@2Pt NCs were studied by XPS. The measurements were done on Kratos AXIS Ultra DLD spectrometer using monochromatic Al source. The spectrometer was calibrated using C *1s* peak at 284.8 eV, Cu $2p_{3/2}$ peak at 932.7 eV and Au $4f_{7/2}$ peak at 83.96 eV as internal standards. The pass energy was fixed at 20 eV for the detailed scans. Typical XPS Fe *2p* and Pt 4*f* spectra are shown in Figure 1a and 1c, respectively. Shifts in the binding energy of Fe and Pt atoms with the changes in the relative Fe to Pt ratio in the NCs are also shown. The shifts are evaluated with respect to the Fe $2p_{3/2}$ (706.9 eV) and Pt $4f_{7/2}$ (71.0 eV) spectral lines characteristic to bulk Fe and Pt, respectively [S3, S4].

As can be seen in Figure 1a, the Fe $2p_{3/2}$ core-level peak position in Fe@1Pt, Fe@1.5Pt and Fe@2Pt NCs is shifted by 0.59 eV, 0.79 eV and 1.19 eV, respectively, in comparison to the bulk value of 706.9 eV. The shift may not be due to oxidation of Fe cores because the Fe $2p_{3/2}$ spectral line in common iron oxides such as Fe_2O_3, involving Fe^{3+} species, Fe_3O_4, involving both Fe^{2+} and Fe^{3+} species, and Fe_xO, involving both Fe^{2+} and Fe^{3+} species, appear at 711 eV, 710.6 eV and 709.5 eV, respectively [S5]. Results of our independent resonant HE-XRD experiments also indicate that Fe cores in Fe@1Pt, Fe@1.5Pt and Fe@2Pt NCs are not oxidized (see Figure S7). The shift may not be due to alloying of Fe and Pt species at the core@skin interface either because prior studies have shown that Fe $2p_{3/2}$ orbitals do not shift up in energy considerably when Fe and Pt atoms intermix at the nanoscale [S6, S7]. On the other hand, studies on Fe NCs and thin layers have found that the Fe $2p_{3/2}$ peak progressively shifts toward a higher binding energy with the diminishing of NC's size and layer's thickness. In particular, the shift has been found to amount to about (+) 1.2-1.5 eV for Fe monolayers and particles with a size less than 2-3 nm. Hence, the observed consistent shift of Fe $2p_{3/2}$ core-level peak position toward higher energy with the thickness of Pt skin may be associated with the respective decrease in the size of Fe cores covered by the skin. Furthermore, the concurrent broadening of the peak can be associated with the so-called "vacancy-cascade" mechanism evoked to explain the XPS spectra of nanosized Fe [S8, S9].

As can be seen in Figure 1c, the Pt $4f_{7/2}$ core-level peak position in Fe@1Pt, Fe@1.5Pt and Fe@2Pt NCs is shifted by -0.34 eV, -0.25 eV and -0.12 eV, respectively, in comparison with the bulk value of 71.0 eV. The shift may not be due to the presence of PtO_x species because the respective Pt $4f_{7/2}$ spectral line would have appeared at about 74.2 eV [S10]. The shift may not be due to alloying of Fe and Pt species at the core-skin interface in the NCs either because prior studies have shown that Pt $4f_{7/2}$ orbitals in Pt-Fe nanoalloys shift up in energy by about 0.5 eV due to Pt↔Fe charge exchange effects in the nanoalloys [S6, S7, S11]. Prior studies on Pt surfaces have related the observed here negative shift in the energy position of Pt $4f_{7/2}$ core-level peak to the inherently reduced coordination of surface Pt atoms as compared to atoms in bulk fcc Pt [S12, S13]. As discussed in the text, the shift of Fe $2p_{3/2}$ and Pt $4f_{7/2}$ core-level peak position toward higher and lower energy, respectively, is related to changes in the valence *d*-electron density of states (DOS) at the Fermi level in Fe core-Pt skin NCs, which, in turn, are related to the different percentage and coordination environment of surface Fe and Pt atoms in the respective NCs.

iv) <u>Electrochemical analyses of Fe core-Pt skin NCs</u>

The catalytic activity of Fe@1Pt, Fe@1.5Pt and Fe@2Pt NCs for oxygen reduction reaction (ORR) was studied using the rotating disk electrode (RDE) technique in 0.1 M $HClO_4$ electrolyte at room temperature. Reference 2.5 nm Pt NCs were also studied. The electrochemically active surface area (ECSA) of the NCs was estimated from cycling voltammetry (CV) curves using the literature value of 210 $\mu C.cm^{-2}$ for polycrystalline Pt. ECSA values ranged from 0.69 m^2g^{-1} for the reference Pt NCs to 0.59 m^2g^{-1}, 0.64 m^2g^{-1} and 0.63 m^2g^{-1} for the Fe@1Pt, Fe@1.5Pt and Fe@2Pt NCs, respectively. Voltammograms recorded at a sweep rate of 5 mV/s showed that the onset potential for Fe@1Pt is 1.02 V and that for Fe@1.5Pt and Fe@2Pt NPs is 1.00 V. The onset potential for pure Pt NCs was found to be 0.98 V. Tafel plots of the specific activity (SA) of Fe core-Pt skin NCs for ORR are shown in Figure S2. The plots clearly show that the kinetics of ORR over Fe core-Pt skin NCs is superior to that over pure Pt NCs in the higher potential range (0.88 V - 0.98 V). In particular, the mass activity (MA) for ORR, which is relevant to practical applications, was found to increase in the order Pt < Fe@2Pt < Fe@1.5Pt < Fe@1Pt NCs. Notably, the MA of Fe@1Pt NPs was found to exceed that of pure Pt NCs by a factor ~ 6. The increase in the MA of Fe@Pt NCs is summarized in Figure 3(d). More details of the electrochemical analyses can be found in ref. [S1].

Without loss of generality, the mechanism of ORR over catalyst surfaces, including catalysts at the cathode of fuel cells, can be described by the following four major steps:

$* + O_2 + H^+ + e^- \rightarrow *OOH$ (S1)

$*OOH + H^+ + e^- \rightarrow *O + H_2O$ (S2)

$*O + H^+ + e^- \rightarrow *OH$ (S3)

$*OH + H^+ + e^- \rightarrow * + H_2O$ (S4),

where (*) stands for catalytically active surface sites, H^+ are protons resulting from splitting of H_2 molecules at the cell's anode and O_2 are oxygen molecules fed to the cell's cathode. It is considered that the likely ORR-rate determining steps are the dissociative adsorption and protonation of molecular oxygen, i.e. step (S1), and removal of reaction intermediates such as atomic oxygen and hydroxyl (OH) groups, in particular step (S4). An efficient catalyst for ORR would bind oxygen molecules with ample strength to allow the cleavage of O-O bonds but weakly enough to liberate the reaction intermediates and product when the reaction completes. In

addition, it is considered that the binding energy of atomic oxygen can serve as an indicator for catalytic activity for ORR [S14-S16]. Pure Pt is the best monometallic catalyst for ORR, even though, according to theory, it binds oxygenated species a bit too strongly by about 0.2 eV [S14, S17]. Our prior work indicated that the superb catalytic activity of Fe@1Pt NCs for ORR can be related to the presence of particular terrace-type sites on the NC's surface that bind oxygen species weaker (by ~ 0.3 eV) as compared to corresponding surface sites in Fe@2Pt and pure Pt NCs [S1]. The particular (~6-fold) improvement of the ORR activity of the former (Fe@1Pt NCs) over that of the latter (reference Pt NCs), though, remained puzzling at the time. Here we find the improvement is proportionate to the increase in the CN_{eff} of surface Pt atoms in the Fe@ Pt NCs with the decrease in the thickness of Pt skin (see data in Figure 3d and related to it text).

v) <u>Characterizing the magnetic properties of Fe core-Pt skin NCs</u>

Magnetic characterization of Fe@Pt NCs was done on a SQUID magnetometer from Quantum Design. Hysteresis curves for Fe@Pt NCs measured at 2 K are shown in Figure S3. Zero field and field (100 Oe) magnetization curves for Fe@Pt NCs are shown in Figure 4a. For an assembly of uniform in shape and well-separated from each other cluster-like Fe particles, that is Fe particles with an average size of less than 2 nm (see EDS maps in Figure 1 and Fe-Fe partial PDFs in Figure 2d), the magnetic anisotropy energy (MEA) may be defined as MEA = K_{eff}V, where K_{eff} and V are the NC's effective anisotropy constant and volume, respectively. In general, the MEA can involve contributions from magnetostatic anisotropy related to the NC's shape, magnetoelastic anisotropy related to atomic-level stresses, anisotropy intrinsic to bcc Fe and surface anisotropy related to the breaking of the 3D periodicity at the NC's surface. Studies have shown that for Fe clusters with a largely spherical shape and size similar to that of Fe cores in Fe@Pt NCs, surface anisotropy is a dominant contributor to the MEA [S18-S20]. Also, studies have shown that the blocking temperature, T_B, effective anisotropy constant, K_{eff}, and volume V for non-interacting superparamagnetic Fe clusters are interrelated as follows [S21, S22]:

$$K_{eff} * V = 25 k_B * T_B \quad \text{(S5)}$$

where k_B is the Boltzman constant and the pre-factor 25 is chosen to account for the typical measuring time, τ, in SQUID experiments (τ ~ 100 s). Using *eq*. S5 and experimental data for T_B (see Figure 4a) and size of respective Fe cores, the effective magnetic anisotropy constant, $K_{eff,}$ for Fe@1Pt, Fe@1.5Pt and Fe@2Pt NPs was found to be 9.2×10^5 J/m^3, 9.09×10^5 J/m^3 and 9.04×10^5 J/m^3, respectively. The values are considerably larger than the intrinsic anisotropy for bulk bcc Fe. The values though are close to K_{eff}=3×10^5 J/m^3 and K_{eff}=5.5×10^5 J/m^3 reported for 2.4 nm inert gas protected and 1.8 nm surfactant coated Fe clusters, respectively [S18, S23]. Besides, they are consistent with the fact that, albeit spherical in shape, the Fe cores are terminated with relatively well-defined facets (see Figure 4b). Note, the large effective anisotropy for Fe@Pt NCs observed here cannot be attributed to interactions between nearby NCs because the values of K_{eff} would vary inversely with the size of Fe cores, but this is not the case. Here it may be added that according to the Stoner-Wohlfarth model for an assembly of non-interaction superparamagnetic clusters, such as Fe cores in Fe@Pt NCs, the coercivity H_c would not depend much on the cluster's size [S24, S25]. This is indeed what our data for the H_c of Fe@Pt NCs show (see Figure S3).

Theoretical work based on a streamlined rectangular *d*-band model [S26, S27] has shown that the magnetic moment, $\mu_{i,}$ of individual atoms in small transition metal clusters, in particular Fe clusters, can be evaluated using the following expression:

$$\mu_{i,} = (CN_{bulk}/CN_{eff}{}^{i})^{1/2} * \mu_{Fe\,(bulk)} \quad if \quad CN_{eff}{}^{i} \geq CN_{bulk} * (\mu_i / \mu_{Fe\,(bulk)})^2$$

$$= \mu_{Fe}(\text{dimer}) \quad \text{otherwise,} \qquad \text{(S6).}$$

Here $\mu_{Fe\,(bulk)} = 2.22\ \mu_B$ and $\mu_{Fe}\,(\text{dimer}) = 3.25\ \mu_B$ are the magnetic moment of Fe atoms in bulk and Fe-Fe dimers, respectively, CN_{bulk} is the number of near neighbors in bulk Fe, and $CN_{eff}{}^{i}$ is the effective coordination number for atom *i* in the considered cluster. Note, for reasons discussed in Section *x)* below, CN_{bulk} was set to 14 and $CN_{eff}{}^{i}$ was computed according *eq. S30.* The average magnetic moment, $<\mu_N>$, per atom of a cluster comprising N atoms was then computed from

$$<\mu_N> = \frac{1}{N} \sum_{i=1}^{N} \mu_i \qquad \text{(S7).}$$

The so-obtained $<\mu_N>$ values are summarized in Figure 4. The values are consistent with predictions of independent theoretical studies on Fe clusters [S69-S71] but not the same. That is because the $<\mu_N>$obtained here are derived from ensemble-average atomic structure data for actual NCs with Fe cores whereas theoretical studies are based on predicted, i.e. not verified experimentally, atomic configurations. The values obtained here are consistent with data from "Stern-Gerlach"-type experiments but not the same either [S16, S58, S66]. That is because the experimental data of Billas et al. [S16, S66] are taken at 120 K whereas, in line with the practices of atomic structure studies, our ensemble-average 3D atomic positions and so $<\mu_N>$ values derived from them are corrected for temperature-related effects (see *eq. S23* below and the related to it text). Hence, as exemplified in Figure S15, the former would appear somewhat diminished in magnitude as compared to the latter.

vi) <u>Resonant high-energy synchrotron XRD (HE-XRD) experiments and derivation of total and element-specific atomic pair distribution functions (PDFs) for Fe@Pt NCs</u>

Carbon supported pure Pu and Fe@Pt NCs were subjected to resonant high-energy synchrotron XRD experiments (HE-XRD) at the 1-ID beamline of the Advanced Photon Source, Argonne. Samples were sealed in thin-walled glass capillaries and measured in transmission geometry. An empty glass capillary, carbon powder alone, bulk fcc Pt and bcc Fe (polycrystalline powder) standards, and 4.5 nm Fe particles, synthesized as described in [S28], were measured separately. The experimental set-up was calibrated with high-purity powder Si standard. Two sets of HE-XRD patterns for each of Fe@Pt NCs were collected using x-rays of two different energies. One of the sets was collected using x-rays with energy of 78.370 keV, which is 25 eV below the K absorption edge of Pt. The other set of patterns was collected using x-rays of energy 78.070 keV, which is 325 eV below the K absorption edge of Pt. X-rays were delivered by a combination of a bent double-Laue monochromator, collimating refracting lenses and a four crystal high-energy resolution (ΔE=8 eV) monochromator [S29]. Scattered x-rays intensities were collected by a solid-state Ge detector coupled to a multi-channel analyzer. A few energy windows, covering several neighboring channels, were set up to obtain x-ray intensities integrated over specific x-ray energy ranges during the data collection, as exemplified in Figure S4. The energy windows covered: the coherent intensities only; the coherent, Compton, and Pt K_β fluorescence intensities

all together; the Pt $K_{\alpha 1}$ and $K_{\alpha 2}$ fluorescence; and the total intensities scattered into the Ge detector. HE-XRD patterns for the respective NCs were collected several times scanning up to wave vectors, q, of 25 Å^{-1} and then averaged to improve the statistical accuracy. HE-XRD patterns for pure Pt and Fe@Pt NCs obtained using x-rays with energy of 78.070 keV are shown in Figure S5 as an example. As can be seen in the Figure, the patterns show a few distinct Bragg-like peaks at low diffraction angles and several broad features at high diffraction angles, i.e. are rather diffuse in nature. This rendered sharp-Bragg peak based techniques for determining the 3D atomic structure of bulk metals and alloys difficult to apply in the case of NCs studied here. Hence, HE-XRD patterns for pure Pt and Fe@Pt NCs were considered in terms of atomic pair distribution functions (PDFs) as described below. For consistency, HE-XRD patterns for bulk fcc Pt and bcc Fe were also considered in terms of atomic PDFs.

In particular, the experimental HE-XRD patterns obtained using x-rays with energy of 78.070 keV were corrected for experimental artifacts (e.g. background scattering) and then used to derive the so-called total structure factors defined as

$$S(q) = 1 + \left[I^{coh.}(q) - \sum c_i \left| f_i\ (q) \right|^2 \right] / \left| \sum c_i\, f_i(q) \right|^2, \qquad \text{(S8)}$$

where $I^{coh.}(q)$ are the coherently scattered intensities extracted from the raw HE-XRD patterns, c_i and $f_i(q)$ are the concentration and x-ray scattering factor, respectively, for atomic species of type i (i=Fe and Pt). The structure factors were Fourier transformed into the so-called total atomic PDFs, G(r), as follows:

$$G(r) = \frac{2}{\pi} \int_{q=0}^{q_{\max}} q[S(q) - 1] \sin(qr) dq\,, \qquad \text{(S9)}$$

where q is the magnitude of the wave vector (q=4πsinθ/λ), 2θ is the angle between the incoming and outgoing x-rays, λ is the wavelength of the x-rays used and r is the radial (real space) distance [S30, S31]. Total atomic PDFs for pure Pt and Fe@Pt NCs are shown in Figure 2a. Total atomic PDFs for bulk fcc Pt and bcc Fe are shown in Figure 2b. Total atomic PDF for 4.5 nm Fe particles is shown in Figure S6. Note, the Fourier transformation is a unitary operation and so does not alter in any way the atomic-structure relevant information contained in HE-XRD data.

By definition, total atomic PDFs reflect all atomic pair correlations in NCs. Hence, the total atomic PDF for Pt NCs shown in Figure 2a reflects correlations between pairs of Pt atoms alone. On the other hand, the total atomic PDFs for Fe@Pt NCs shown in the same Figure are a weighted sum of 3 partial atomic PDFs G_{ij}(r), in particular $G_{Fe\text{-}Fe}$(r), $G_{Fe\text{-}Pt}$(r) and $G_{Pt\text{-}Pt}$(r) partial PDFs, that is:

$$\mathrm{G(r)} = \sum_{i,j} w_{ij} G_{ij}(r)\,, \qquad \text{(S10).}$$

where c_i, and $f_i(q)$ are the concentration and x-ray scattering factor of the particular atomic species, and the weighting factors w_{ij} are defined as:

$$w_{ij} = c_i c_j f_i(q) f_j(q) / [\sum c_i\, f_i(q)]^2 \qquad \text{(S11).}$$

To determine the contributions of $G_{Fe\text{-}Fe}$(r) partial PDFs to the total PDFs for Fe@Pt NCs, the so-called Pt-differential atomic PDFs were obtained at first as follows [S34]:

$$DS(q)_{Pt} = \frac{I^{coh}(q,E_1) - I^{coh}(q,E_2) - [< f^2(E_1) > - < f^2(E_2) >]}{< f(E_1) >^2 - < f(E_2) >^2} + 1 \quad \text{(S12)}$$

where E_1 and E_2 denote the data sets collected using x-rays with energy of 78.070 keV and 78.370 keV, respectively, the atomic scattering factors f(E) = f_o(q) + f'(q, E) + if"(q, E), and f' and f" are the so-called dispersion corrections [S32, S33]. Then, Pt-differential atomic PDFs, $DG(r)_{Pt}$, were obtained via a Fourier transformation as given below:

$$DG(r)_{Pt} = \frac{2}{\pi} \int_{q=0}^{q_{max}} q[DS(q)_{Pt} - 1]\sin(qr)dq \quad \text{(S13).}$$

Note, the Pt-differential atomic PDFs comprise contributions from Pt-Pt and Pt-Fe atomic pairs because only the scattering factor of Pt species changes significantly when resonant HE-XRD experiments are done at the Pt K edge, *i.e.*

$$DG(r)_{Pt} = \sum_i \Delta w_{Pt-i} G_{Pt-i}(r) \quad \text{(S14)}$$

where

$$\Delta w_{Pt-i} = \frac{c_{Pt} c_i \ \mathrm{Re}[f_i(f_{Pt}^*(E_1) - f_{Pt}^*(E_2)]}{< f(E_1) >^2 - < f(E_2) >^2} \quad , \quad \text{(S15).}$$

Here c_i is the concentration of atomic species of type *i* and *f*(E)* is the complex conjugate of *f(E)*. Finally, by using the so-called MIXSCAT approach, the Fe-Fe partial PDFs for Fe@Pt, Fe@1.5Pt and Fe@2Pt were obtained from the respective total and Pt-differential PDFs as follows [S34]:

$$\text{Fe-Fe partial PDF} = [\text{respective Total G(r)}/w_{ij} - [\text{respective DG(r)}_{Pt}]/\Delta w_{Pt-i} \quad \text{(S20)}$$

where w_{ij} and Δw_{Pt-i} are the weighting factors of Pt-Pt and Pt-Fe atomic pairs computed using *eqs. (S11)* and *(S14)*, respectively. The resulting partial G_{Fe-Fe}(r)s are shown in Figure 2d. More details of resonant HE-XRD experiments and derivation of element-specific atomic PDFs can be found in ref. [S35]. Evidence for the sensitivity of resonant HE-XRD to the distribution of chemical species in metallic NCs can be found in refs. [S36, S37]

vii) Crystal-structure Constrained Modeling

To ascertain the quality of HE-XRD experiments and atomic PDFs derivation, the total PDFs for bulk Fe and Pt powder standards were fit with models constrained to an bcc- and fcc-type crystal structure adopted by bulk Fe and Pt, respectively [S38]. The initial models perfectly 3D periodic, infinite lattices of the respective structure type. The δ-functions-like peaks in the atomic PDFs derived from the models were broadened by convolution with Gaussian functions as to mimic the usual broadening of the atomic coordination spheres in metallic nanomaterials at ambient conditions. The unit cell parameters of the model lattices were adjusted such that model-derived atomic PDFs approached the corresponding experimental ones as closely as possible. The modeling was done with the help of the program PDFgui [S39]. Results from the modeling are shown in Figure 2b. As can be seen in the Figure, the experimental PDF data are reproduced very well by the respective 3D model lattices. The refined lattice parameters, a=2.869 Å for bcc Fe, and a= 3.921 Å for fcc Pt, compare very well with literature data (a=2.867 Å for bulk Fe and

3.923 Å for bulk Pt) [S38]. Results attest to the very good quality of the present synchrotron HE-XRD experiments.

To ascertain the phase state of Fe cores, the experimental Fe-Fe partial PDFs for Fe@Pt NCs were approached with models based on the atomic structure of common Fe^{+2} and Fe^{+3}–based oxides, including wustite, hematite and magnetite. The models made sense since Fe is known to be highly reactive towards oxygen under ambient conditions. Modeling was done with the help of the program PDFgui. Models were based on crystal structure data for wustite, hematite and magnetite obtained from literature sources [S40]. Results of the modeling, that is nothing but "phase-analysis" by XRD, are shown in Figure S7. As can be seen in the Figure, experimental Fe-Fe partial PDFs do not show features characteristic to common Fe oxides. Thus, in line with the findings of XPS experiments, HE-XRD experiments indicated that Pt skin of Fe@Pt NCs largely protects Fe cores from oxidation.

viii) *Molecular Dynamics simulations*

3D atomic models for 4.5 nm pure Fe particles, 2.5 nm pure Pt and Fe@Pt NCs were built by classical Molecular Dynamics (MD) simulations based on the quantum-corrected Sutton-Chen (Q-SC) potential [S41-S43]. It considers the energy of atomic-level models, *E,* as a sum of an atomic pair potential $P(r_{ij})$ term and a local electron density (ρ_i) term defined as follows:

$$E = \sum_i \left[\sum_{j \neq i} \frac{1}{2} h_i * \epsilon_{ij} * P\left(r_{ij}\right) - s_i * \epsilon_{ij} * (\rho_i)^{\frac{1}{2}} \right] \quad \text{(S21)}$$

where

$$P\left(r_{ij}\right) = \left(\frac{a_{ij}}{r_{ij}}\right)^{n_{ij}} \text{ and } \rho_i = \sum_{j \neq i} \left(\frac{a_{ij}}{r_{ij}}\right)^{m_{ij}} \quad \text{(S22).}$$

The so-called "energy" parameter $\epsilon_{ij}(meV)$ and the dimensionless parameter s_i are used to scale appropriately the strength of repulsive $P(r_{ij})$ and attractive (ρ_i) metal-to-metal atom interactions, respectively. Parameters m_{ii} and n_{ii} are positive integers such that $n_{ii} < m_{ii}$. The parameter a_{ij} is a quantity used to scale distances r_{ij} between *i* and *j* type atoms in the structure models. Typically, values of a_{ij} are calibrated against the lattice parameter for the respective bulk metals. SC parameters for Fe and Pt were taken from literature sources [S43, S44].

In general, the realism of MD simulations depends both on the type of structure models chosen and conditions under which the simulations are run. Hence, to be as realistic as possible, the initial model atomic configurations for pure Pt and Fe@Pt NCs reflected the average size (~ 2.5 nm), shape (polyhedral) and chemical composition (Fe_xPt, where x=0, 0.4. 07 and 1.2) of the NCs modeled. Accounting for the diffraction features of experimental HE-XRD patterns and phase diagrams of bulk Fe, Pt and Fe-Pt alloys, several types of structure models were considered. In particular, for the Fe@Pt NCs we considered models based on a fcc-type structure alone and models wherein Fe and Pt atoms maintain the structure type of their bulk counterparts, that is, bcc for Fe and fcc for Pt [S38]. An fcc-type model (2.5 nm in size) for pure Pt NCs with the respective size (2.5 nm) and a bcc-type model for pure Fe particles with the respective size (4.5 nm) were also generated. All initial atomic configurations were optimized in terms of energy, i.e. stabilized at atomic level, with the help of the computer program DL-POLY [S45]. The optimization was performed under canonical NVT ensemble in the absence of periodic boundary conditions. Velocity Verlet algorithm with a time step of 2 fs was used.

Typically, MD simulations on metallic systems involve quenching of atomic configurations equilibrated at very high temperature. However, as it is the common practice in nanotechnology, Fe@Pt NCs were synthesized in solution, i.e. they were not obtained by rapid quenching from a melt. Hence, the initial atomic configurations used in the MD simulations were not melted but equilibrated for 150 ps at 400 ^{o}C, cooled down to room temperature in steps of 50 K and again equilibrated for 150 ps. Results from MD simulations of 4.5 nm Fe particles and 2.5 nm Pt NCs are shown in Figure S8. Results from MD simulations featuring Fe@Pt NCs with an overall fcc-type atomic structure are presented in Figures 2a and S9. Results from MD simulations featuring Fe@Pt NCs with a bcc-type Fe core nested inside a tight fcc Pt shell are shown in Figure S10. Data in Figure S8 indicate that the atomic ordering in pure Fe and Pt particles is bcc- and fcc-like, respectively. However, as can be seen in Figurs 2a and S9, models for Fe@Pt NCs based on a structurally coherent fcc Fe core and fcc Pt shell do not reproduce the experimental PDF data well, in particular the intensities of several major PDF peaks. The observation indicates that, though exhibiting HE-XRD patterns similar to that of fcc Pt NCs (see Figure S3), Fe@Pt NCs may not be described as stacks of close packed atomic layers known to occur with fcc Pt and Fe_xPt alloys, where x is in the range from 0.4 to 1.2 [S38, S46]. On the other hand, as data in Figure S10 show, models for Fe@Pt NCs based on a bcc Fe core and fcc Pt skin, that are incommensurate in terms of atomic packing efficiency and near neighbor coordination, reproduce the experimental PDF data reasonably well. For reference, contrary to the fcc-type structure which involves both close packed $(111)_{fcc}$ atomic layers and $<110>_{fcc}$ directions, the bcc-type structure does not involve close packed atomic layers but close packed $<111>_{bcc}$ directions alone [S38]. Accordingly, the atomic packing fraction (68 % vs 74 %) and near-neighbor coordination (8 + 6 vs 12; see Figure 2b) in bcc-and fcc-type structure are significantly different. The advantage of bcc Fe@fcc Pt structure model over the fcc Fe@fcc Pt one becomes even more evident when Fe-Fe partial PDFs derived from the models are compared with the respective experimental data sets, as demonstrated n Figure S11. Hence, the former model was considered as a plausible 3D atomic structure of Fe@Pt NCs studied here and refined further against the experimental total and Fe-Fe partial PDFs by reverse Monte Carlo (RMC). The bcc- and fcc-type structure models for pure Fe particles and Pt NCs, respectively, were also refined by RMC, as described below.

ix) Reverse Monte Carlo Refinement of the MD models

Best MD models for 4.5 nm Fe particles, 2.5 nm Pt and Fe@Pt NCs were refined further by RMC simulations guided by the respective total and partial Fe-Fe atomic PDFs [S47]. The refinement was necessary since actual metallic NCs exhibit local structural relaxation, in particular close to their surface, and chemical patterns which may not be captured by MD alone, i.e. without experimental input. Note, as demonstrated in Figures 2c, 2d, S7, S9, S10 and S11 and work of others atomic PDFs are sensitive to the length of structural coherence, that may or may not be comparable to the NC size, and phase composition (e.g. oxidized vs metallic, bcc vs fcc vs metallic glass-like structure) of metallic NCs [S48-S51]. Dewtails of the refinementare described below:

i) It is well-known that atoms in metallic materials can experience both random atomic displacements, also known as (Debye-Waller type) thermal vibrations, and static displacements, i.e. relax. Hence, to decouple the latter from the former, peaks in the total and partial PDFs computed from the RMC-refined models were convoluted with a Gaussian broadening function,

$$F(r) = \frac{1}{\sigma_T\sqrt{2\pi}} * \exp(-\frac{r^2}{2\sigma_T^2}) \quad \text{(S23)}$$

where r is the radial distance and σ_T is the thermal root-mean-square (rms) displacement of either Fe or Pt atoms at room temperature. The respective values of σ_T were taken from literature sources [S40].

ii) During the refinement, positions of atoms in the MD-optimized atomic configurations were adjusted as to minimize the difference between the RMC-computed and experimental total partial atomic PDFs. Normalized distribution of Pd-Pd bonding distances in pure Pt and Fe@Pt NCs, computed from the adjusted atomic positions, are reported in Figure 3b.

iii) Simultaneously, the RMC refinement was frequently switched between two modes of operation exemplified in Figure S12. That is, the experimental atomic PDF data were represented either in terms of G(r) or r*G(r) so that the distinctive atomic-level features of both the interior and near-surface region of the NCs modeled were captured in due detail.

iv) In addition, atoms in the refined 3D structures were required (i.e. restrained but not constrained) not to come much closer than pre-selected distances of closest approach, thereby taking into account the fact that individual atoms in metallic materials may share valence electrons but remain distinct entities.

v) Last but not least, the energy of the refined models was minimized further, i.e. beyond the level already achieved by MD, using pair-wise potentials taken from literature sources [S52].

Altogether, RMC refinements aimed at minimizing a residuals function χ^2 involving two major terms, χ^2_Ω and χ^2_Θ, defined as as follows [S53]:

$$\chi^2_\Omega = \frac{\sum[G(tot)_i^{\exp} - G(tot)_i^{calc}]^2}{\varepsilon^2_{G(r)}} + \frac{\sum[G(Fe-Fe)_i^{\exp} - G(Fe-Fe)_i^{calc}]^2}{\varepsilon^2_{G(r)}} + \frac{\sum[R_{ij}^{des} - R_{ij}^{calc}]^2}{\varepsilon^2_{R_{ij}}} \quad \text{(S24)}$$

$$\chi^2_\Theta = \frac{\Delta U}{\varepsilon^2_{\Delta U}} \quad \text{(S25)}$$

where $G(tot)_i^{exp}$ and $G(tot)_i^{cal}$, $G(Fe\text{-}Fe)_i^{exp}$ and $G(Fe\text{-}Fe)_i^{exp}$ are model-derived and experimental total and Fe-Fe partial atomic PDFs for a given value of the real space distance r_i, respectively, and R_{ij}^{des} and R_{ij}^{cal} are preset plausible (see above) and model calculated ij atomic pair distances of closest approach, respectively. Understandably, both total and Fe-Fe partial atomic PDFs participated in *eq. S24* in the case of Fe@Pt NCs whereas total PDFs alone were fit in the case of pure Fe particles and Pt NCs. The term ΔU reflects changes in model's energy as described by pair-wise potentials (see above). The ε*'s* in the denominators of *eqs. S24* and *S25* are weighting factors allowing controlling the relative importance of the individual terms in the residuals function χ^2 being minimized. In the course of refinements the values of ε*'s* and rate of switching between the two modes of RMC operation exemplified in Figure S12 were changed several times to increase the chances of finding the global minimum of the residuals function χ^2, instead of a local minimum. Note, using constraints, restraints, penalty functions etc. is a common practice in refining 3D structure models against diffraction data [S53-S57]. Those though are used to guide the refinement and not to pre-determine its outcome. The major goal of the refinement is to find a 3D structure that both reproduces the experimental diffraction data in

very good detail and does not contradict any other available piece of structure-relevant information (e.g. overall chemical composition, morphology, structure type as optimized by MD, etc.) for the NCs under study. Hence, the RMC refinements were considered complete when their major goal was achieved, including the minimization of the residuals function χ^2. Computations were done with the help of a newer version of the program RMC++ allowing refining full-scale models for metallic NPs of any size and shape under non-periodic boundary conditions [S54].

MD-optimized models for pure Pt and Fe@Pt NCs converged to the atomic configurations shown in Figure 3a. The MD-optimized MD model for 4.5 nm Fe converged to the atomic configuration shown in Figure S6(see the inset). As can be seen in the Figures 2c, 2d, and S6, atomic PDFs derived from the refined configurations reproduce the respective experimental data sets in very good detail. The overall quality of the configurations was quantified by computing a goodness-of-RMC-fit indicator defined as

$$R_w = \left\{ \frac{\sum w_i (G_i^{\exp.} - G_i^{calc.})^2}{\sum w_i (G_i^{\exp.})^2} \right\}^{1/2} \qquad \text{(S26)}$$

where $G^{exp.}$ and $G^{calc.}$ are the experimental and RMC-fit atomic (total and Fe-Fe) PDFs, respectively, and w_i are weighting factors reflecting the experimental uncertainty of individual experimental data points. Here w_i were considered to be uniform which, as predicted by theory [S55] and corroborated by experiment [S56], is a reasonable approximation. The R_w values of about 7 (± 3) % for the RMC-fits shown in Figures 2c, 2d and S6 certify the high quality of the respective 3D atomic configurations. Here it is to be underlined that the configurations are generated by MD, refined by RMC and evaluated (see *eq. S26*) strictly following the successful practices of determining the 3D atomic structure of metallic materials, including fine powders, by x-ray scattering techniques [S57]. The comparison with the latter is particularly fair since determining the 3D structure both of polycrystalline and nanocrystalline metallic particles, such as pure Pt and Fe@Pt NCs studied here, rely on diffraction datasets obtained from ensembles of entities with a fairly close chemical composition, size and shape. As such, within the limits of the experimental accuracy, the RMC refined 3D atomic configurations shown in Figures 3a and S6 can be considered as the most likely 3D atomic structure of the respective NCs [S53, S55-57], and so are fit for their purpose. That is, the structures can provide a sound basis for assessing the structure-function relationship for the respective NCs, as done in Figures 3d and 4c. Note, atomic configurations with an overall chemical composition different from that determined by ICP-AES cannot be considered as likely 3D atomic structures of Fe@Pt NCs. Planar, rod, frame-type atomic configurations and atomic configurations that are with a size substantially different from 2.5 nm cannot be considered as likely 3D atomic structures of Fe@Pt NCs either since such configurations would contradict the experimental HAADF-STEM and PDF data (see Figures 1, S1 and 2).

ix) Assessing the local atomic structure in Fe cores and Pt skin in terms of effective coordination numbers CN_{eff}

The reactivity of Pt surfaces and magnetic properties of Fe clusters are largely determined by the width, w_d, and energy position, ε_d, of surface *d*-electron bands with respect to the Fermi energy, degree of hybridization of valence *s*, *p* and *d* electrons of surface Pt atoms and the resulting number and character of valence electrons at the Fermi level, often represented in terms of

electron density of states (DOS) near the Fermi energy [64-66]. In general, according to electronic structure theory of metals, w_d is proportional to the number of nearest neighbor atoms, that is the first coordination number (CN), as follows:

$$w_d = \mathrm{CN}_{*}.\sqrt{\beta(r_{ij})^2}, \quad \text{(S27)}.$$

Here β represents the average hopping probability of a *d*-electron from one metal atom to another, assuming only the near neighbor hopping. The CN of surface atoms, CN(surf), though is greatly reduced as compared to that of atoms in the respective bulk, i.e. CN(bulk). Hence, the *d*-band width, w_d^s, of surface atoms narrows considerably. As shown by theory [S16, S26],

$$w_d^s \sim w_{d(bulk)*}\sqrt{\frac{CN(suf.)}{CN(bulk)}} \quad \text{(S28)}.$$

Furthermore, the energy position of the *d*-band for surface atoms, ε_d^s, also changes as follows

$$\varepsilon_d^s = \varepsilon_{d(bulk)} + \frac{E(coh)}{2\theta_d} * (\frac{CN(surf)}{CN(bulk)} - 1)\ , \quad \text{(S29)}$$

where *E(coh.)* is the cohesive energy of a bulk atom and Θ_d is the degree of filling of the *d*-band. Thus, it is straightforward to conclude that changes in the coordination of surface atoms would modify greatly the reactivity of Pt surfaces and magnetism of Fe clusters, where the surface to volume ratio is very high. Therefore, as shown in work of others [S26, S27, S67, S68], the former (atomic coordination) may be used to evaluate the latter (reactivity and magnetic propertiez). To capture the dependence of physicochemical properties of surfaces and clusters on the coordination of surface atoms in better detail, the use of an effective CN, $\mathrm{CN}_{\mathrm{eff}}$, has proven very useful. It is defined as

$$\mathrm{CN}_{\mathrm{eff}}\,(\mathrm{i}) = \sum_{i=1}^{n} \frac{CN(j)}{CN_{max}}, \quad \text{(S30)}$$

where the sum includes all *j* near-neighbors of a surface atom *i*, and the division by the maximum coordination number, $\mathrm{CN}_{\mathrm{max}}$, characteristic for the respective structure gives a weight of the contribution of nearby atoms to the coordination of the surface atom under consideration. Note that computing and using $\mathrm{CN}_{\mathrm{eff}}$ is similar to the embedded atom method (EAM) in a sense that the charge density at a surface site is approximated by a superposition of charge densities of the nearest neighbors which, in turn, depend on the charge densities of their near neighbors. In the EAM and other models based on the "atom in jellium" concept, the superposing contributions from neighboring atoms have an exponential form and are averaged over a sphere at the surface sites so that a local charge balance (continuity of the Fermi level) is achieved. Often, the sphere coincides with the so-called Wigner-Seitz sphere associated with the "size" of atom occupying the surface site under consideration [S72-S74].

In computing the $\mathrm{CN}_{\mathrm{eff}}$ for Pt atoms forming the very thin skin of Fe@Pt NCs we used the bulk diameter/size of Pt atoms (2.775 Å) as a near-neighbor distances and $\mathrm{CN}_{\mathrm{max}}$ was set to 6. The latter is the maximum possible CN for Pt atoms occupying a close-packed $(111)_{\mathrm{fcc}}$ monolayer. The distribution of near-neighbor distances between the individual surface Pt atoms in Fe@Pt NCs, as normalized against the bulk value, is summarized in Figure 3b. The evolution of the $\mathrm{CN}_{\mathrm{eff}}$ for surface Pt sites in Fe@Pt NCs with the skin thickness is exemplified in Figure 3c and quantified in Figure 3d (see the respective bars). In computing the $\mathrm{CN}_{\mathrm{eff}}$ for Fe atoms forming the cores in Fe@Pt NCs we used the first physical minimum of the experimental Fe-Fe

partial PDFs as a near neighbor distance (3.20 Å). Thus we accounted for the observed relaxation of Fe atoms forming the cores that virtually leads to merging of the first (8 neighbors) and second (six neighbors) coordination spheres occurring in bulk bcc Fe. Accordingly, we set CN_{max}=14. Note, the first (radius R_1) and second (radius R_2) coordination spheres in fcc Pt are considerably separated from each other, that is, $R_2(fcc) = \sqrt{2}*R_1(fcc)$ (~ 41 % difference). By contrast, those for bcc Fe are rather close to each other, that is $R_2(bcc) = 1.15*R_1(bcc)$ (15 % difference) and so are likely to come even closer together in Fe clusters comprising a few hundreds of atoms alone. Arrows in Figure 4b represent magnetic moments of individual Fe atoms in Fe@Pt NCs below T_B, as computed from *eq. S6* involving the foregoing CN_{max} and CN_{eff}. Arrows in Figure S15 represent magnetic moments of individual Fe atoms in Fe@Pt NCs at temperature well above T_B. The evolution of the CN_{eff} and so average $<\mu>$ (in μ_B) for Fe atoms with the radial distance, R, from the center of Fe cores in Fe@Pt NCs is shown in Figure 4c. Contrary to the finding of others [S59], the values of $<\mu>$ are seen to converge smoothly toward the bulk value of 2.22 μ_B with diminishing R.

x) Evaluating the size dependence of $<\mu(N)>$ of Fe cores

By adopting a spherical cluster model, it may be conjectured that for a spherical cluster comprising *N* atoms, the ratio of surface to total number of atoms is about $3N^{-1/3}$ and so the cluster-size dependence of the average magnetic moment per atom in Fe clusters would be

$$<\mu(N)> = \mu_{Fe} + (\mu_{surf} - \mu_{Fe})*3N^{-1/3} \qquad \text{(S31)}.$$

Here μ_{Fe} and μ_{surf} are the magnetic moment of Fe atoms in bulk (2.22 μ_B) and at the open surface of Fe clusters respectively. Furthermore, based on experimental findings [S58], it may be conjectured that surface Fe atoms are in $3d^74s^1$ state and have their majority *d*-band entirely below the Fermi level, thus occupied by five *3d*-electrons in spin up state. Accordingly, the minority *d*-band is occupied by two *3d*-electrons in spin down state. Then, $\mu_{surf} = 3\ \mu_B$. A comparison with $<\mu(N)^{exp}>$ data obtained by "Stern-Gerlach" type experiments [S19, S66] though shows that the convergence of $<\mu(N)>$ to the bulk value with increasing *N* is not as uniform and slow as predicted by *eq. S31* (see Figure 4c). Note that in deriving $<\mu(N)^{exp}>$ values, it has been considered that the dependence of $<\mu(N)^{exp}>$ on the applied external magnetic field and temperature may well be described as follows:

$$M/<\mu(N)^{exp}> = L(<\mu(N)^{exp}>* N* H/(k_B*T). \qquad \text{S(32)}$$

Here M is the measured magnetization for clusters comprising N atoms, H is the external magnetic field, k_B is the Botlzmann constant and T is the temperature at which M has been measured. Also, L(x) = coth(x)-1/x is the so-called Langevin function with an argument $x=<\mu(N)^{e-p}>* N* H/(k_B*T)$. Evidently, the model based on *eq. S31* is too simple to account for the observed cluster-size (N) dependence of $<\mu(N)>$. Other models assuming that all Fe clusters with given N appear as a particular polyhedron with uniform facets, including truncated decahedron, cuboctahedron, rhombic dodecahedron and others based on the concept of geometric shell clusters, fail in describing the observed dependence of$<\mu(N)>$ on N either [S59-S61]. Largely, that is because such models ignore the ensemble-average nature of $<\mu(N)^{exp}>$. That is, the models do not take into account the fact that, due to the intrinsically broken 3D periodicity of surface atomic arrangement, metallic clusters with the same size (N) may co-exist as various

isostructural polymorphs wherein corresponding surface atoms differ in CN_{eff} [74] and so in magnetic moment. Thus, clusters with the same size (N) may show a somewhat different $<\mu(N)^{exp}>$ and clusters with somewhat different size (N) may show virtually the same $<\mu(N)^{exp}>$. A more realistic approach is to take into account the ensemble-average nature of $<\mu(N)^{exp}>$ and describe its functional dependence on N as follows:

$$<\mu(N)> = \mu_{Fe} + (\mu_{Fe(\text{dimer})} - \mu_{Fe}) / \left(1 + e^{\left(\frac{N-N_0}{\Delta N}\right)}\right), \quad \text{(S33)}$$

where $\mu_{Fe} = 2.22\ \mu_B$ and $\mu_{Fe(\text{dimer})} = 3.2\ \mu_B$ is the magnetic moment of Fe atoms in bulk and Fe-Fe dimers (N=2), respectively, N_o is the so-called point of symmetry where $<\mu(N)> = \mu_{Fe} + (\mu_{dim} - \mu_{Fe})/2$, and the empirical parameter ΔN is the rate of change of $<\mu(N)>$ with N [S20, S61, S62]. As data in Figure 4c show, the experimental data of Billas et al. [S19, S66] taken at T=120 K can be fit well (R^2=0.92) with the function described by *eq. S33*. The fit returns μ_{dim} = 2.98(8) μ_B, μ_{Fe} = 2.26(6) μ_B, N_o = 283(2) and ΔN=86(1). The values of $<\mu(N)>$ for Fe@Pt NCs derived here can also be fit well (R^2 =0.89) with the function described by *eq. S33*. The fit returns $\mu_{Fe(\text{dimer})}$ = 3.22(1) μ_B, μ_{Fe} = 2.25(1) μ_B, N_o = 350(3) and ΔN=105(5). As discussed in Section *iv)* above, the higher value for $\mu_{Fe(\text{dimer})}$ (3.2 μ_B vs 2.98 μ_B) matching the $<\mu_N>$ values obtained here may be explained by temperature-related effects. Here it is to be noted that a function of the type 1/(1+exp(-x)) used to describe the ensemble-average nature of $<\mu_N>$ for superparamagnetic Fe clusters (second term in *eq. S33*) has a sigmoid shape much like the Langevin function appearing in *eq. S32*. Indeed sigmoid and hyperbolic functions of the type appearing in *eqs. S32 and S33* are related as follows:

$$1/(1+\exp(-x)) - 1/2 = 1/2 * \tanh(x/2), \quad \text{(S34)}.$$

and $\tanh(x) = \coth^{-1}(x)$.

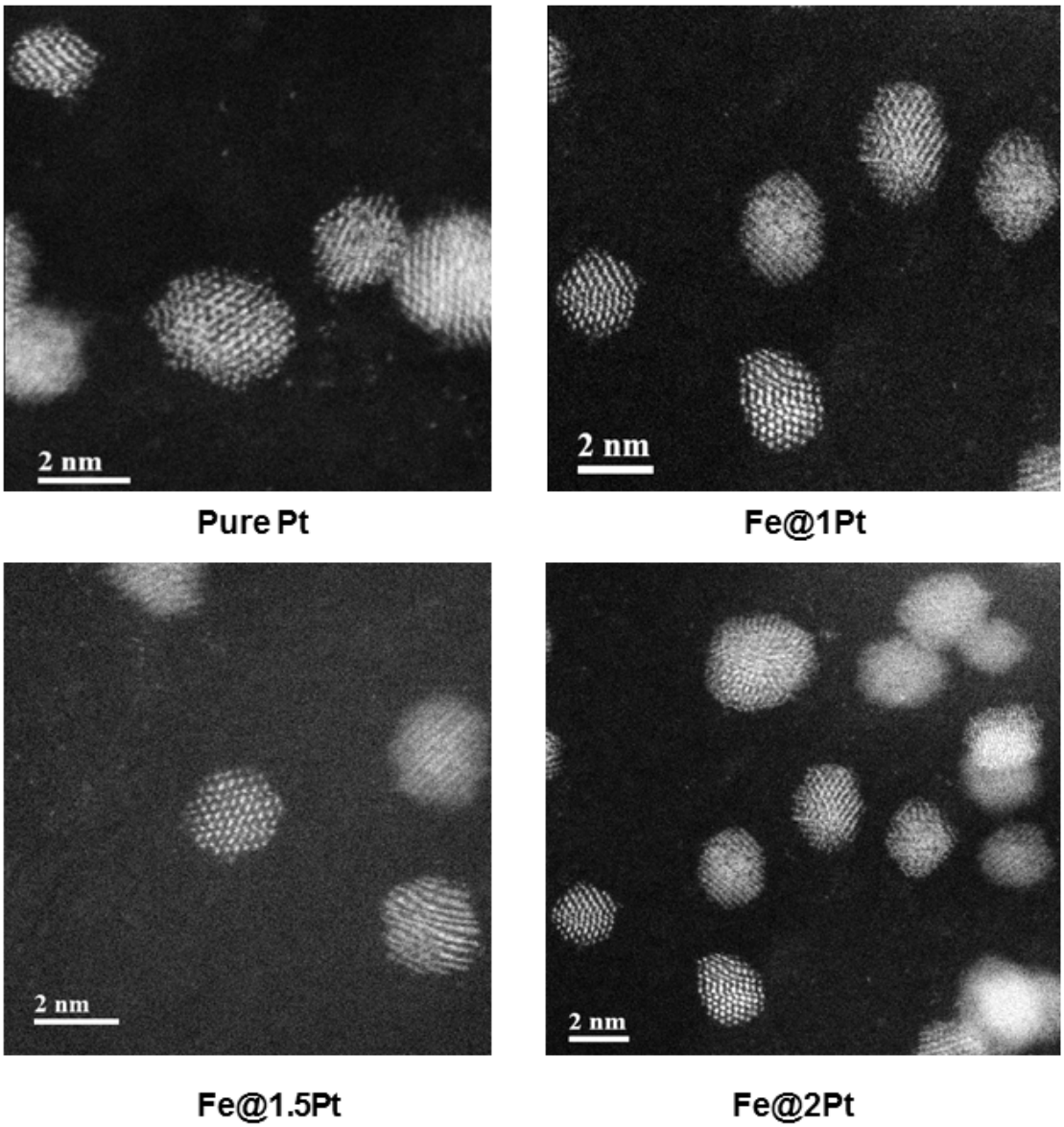

Figure S1. Representative HAADF-STEM images of pure Pt, Fe@1Pt, Fe@1.5 Pt and Fe@2Pt NCs. The NCs appear with an average size of approximately 2.5(± 0.3) nm and exhibit lattice fringes evidencing their (nano)crystalline nature.

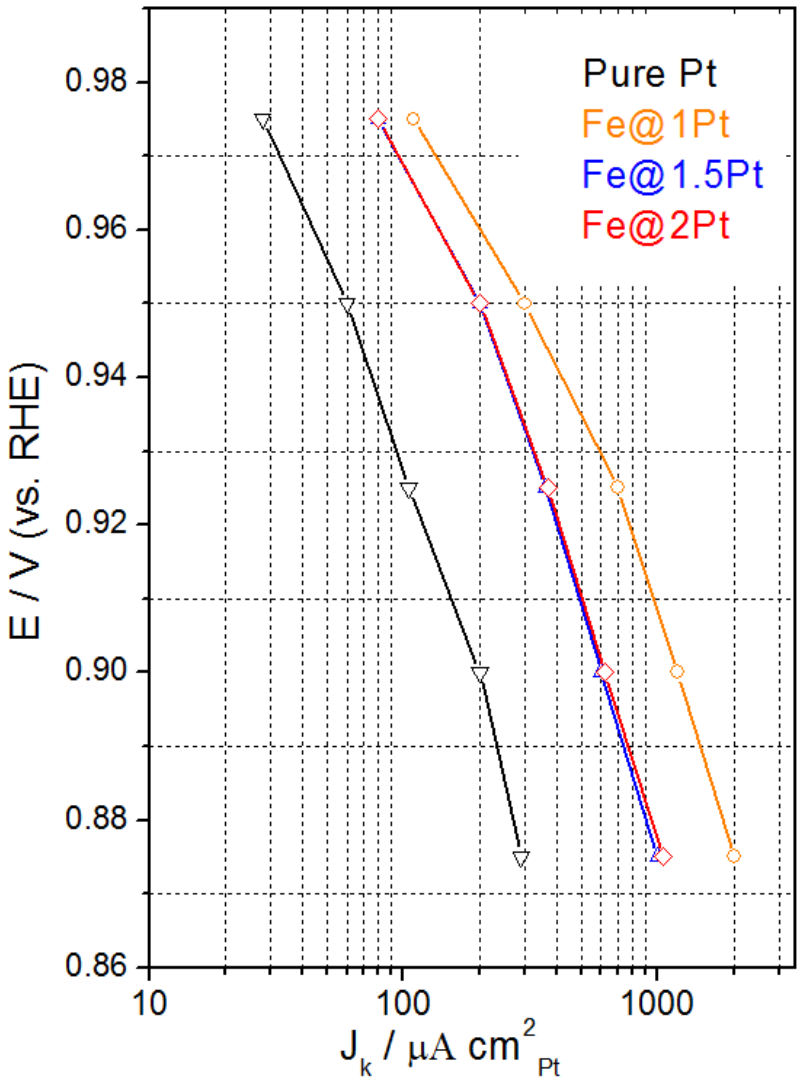

Figure S2. Tafel plots for pure Pt and Fe@Pt NCs measured in an O_2-saturated 0.1 M $HClO_4$ electrolyte [S1]. Note data in the plot are normalized by experimental ECSA values and amount (mass) of Pt in the respective NCs, for better comparison.

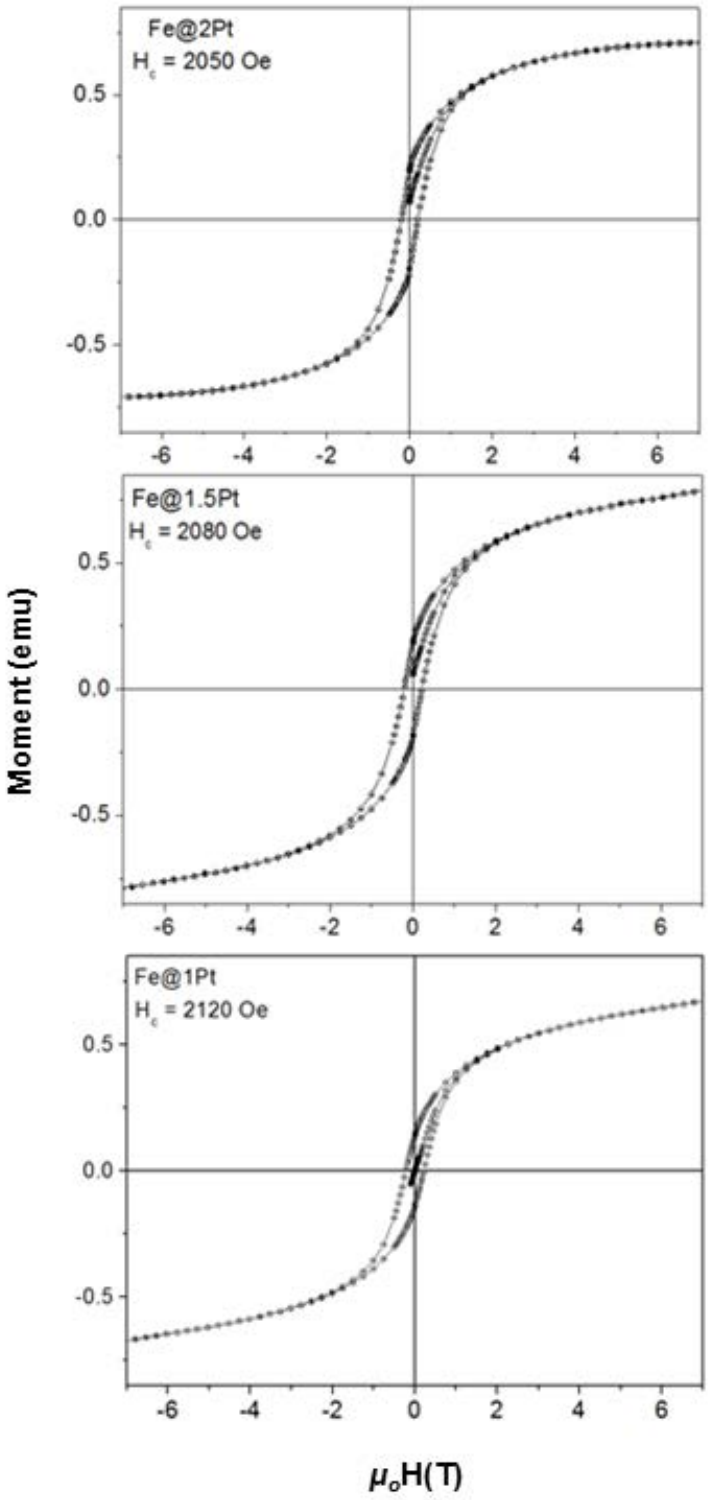

Figure S3. Hysteresis curves for Fe@Pt NCs measured at T=2 K. Coercivity, H_c, is given for each data set.

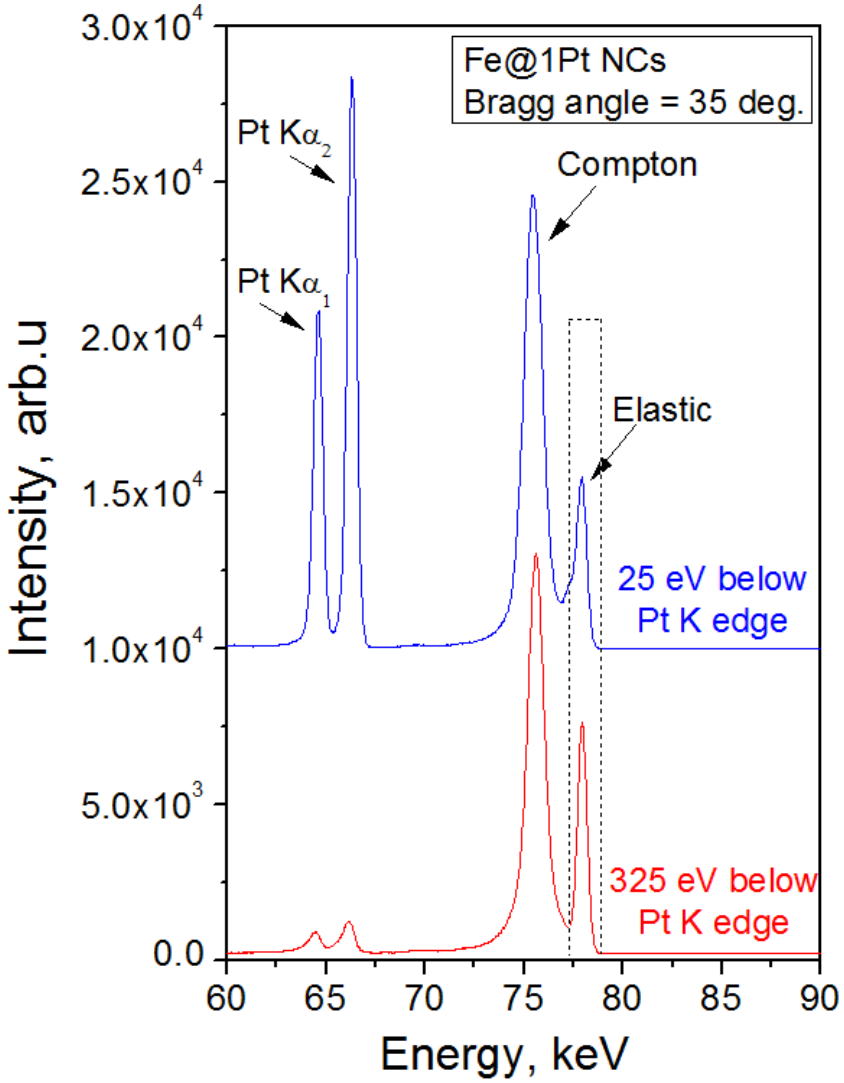

Figure S4. X-ray energy sensitive spectra for Fe@1Pt NCs obtained at a fixed diffraction (Bragg) angle of 35 deg. Spectra are obtained using x-rays with energy of 78.070 keV (red line) and 78.370 keV (blue line). The first energy is 325 eV below and the second energy is 25 eV below the K absorption edge of Pt (78.395 keV). Elastically and inelastically (Compton) scattered intensities as well as Pt ($K\alpha_1$ + $K\alpha_2$) fluorescent lines are marked with arrows. The difference between two XRD patterns including the elastically scattered intensities only, i.e. the intensities falling into the "x-ray energy window" outlined with a broken line, was used to derive (see *eq*. S16) the Pt-differential structure factors for Fe@Pt NCs.

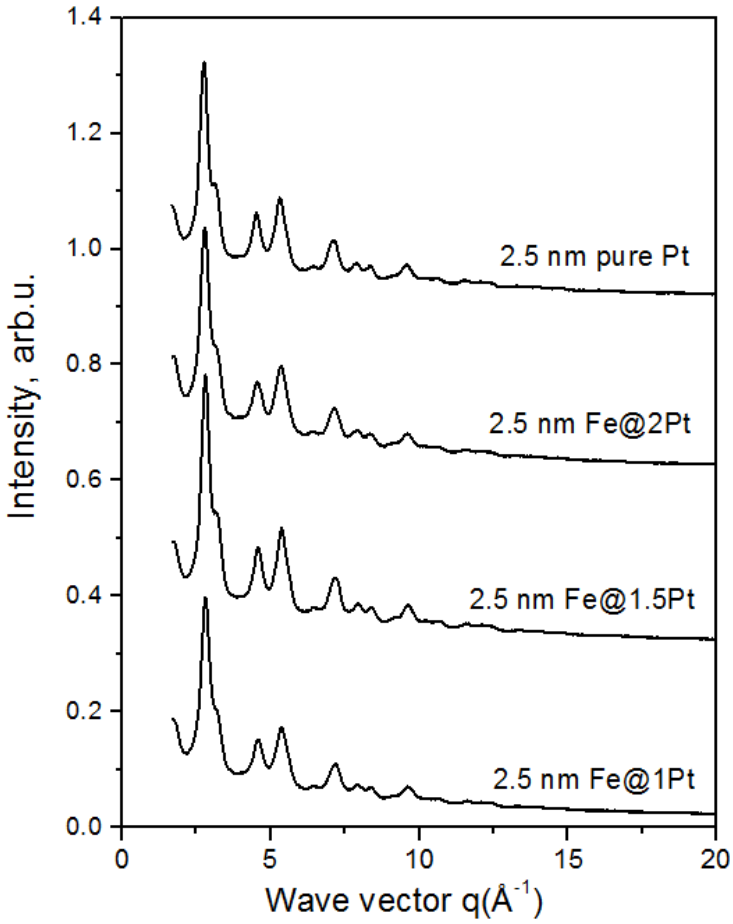

Figure S5. Experimental HE-XRD patterns for 2.5 nm Pt, Fe@1Pt, Fe@1.5Pt and Fe@2Pt NCs obtained using x-rays with energy of 78.070 keV. Note, HE-XRD patterns and so their Fourier counterparts, the atomic PDFs, reflect ensemble averaged structural features of all NCs sampled by the x-ray beam in a way traditional powder XRD patterns reflect ensemble averaged structural features of all polycrystallites sampled by the x-ray beam in those experiments. Using NC ensemble-averaged 3D atomic positions to understand and explain NC ensemble-averaged functional properties, such as catalytic, magnetic, optical and others, puts the NC atomic structure- functional properties exploration on the same footing.

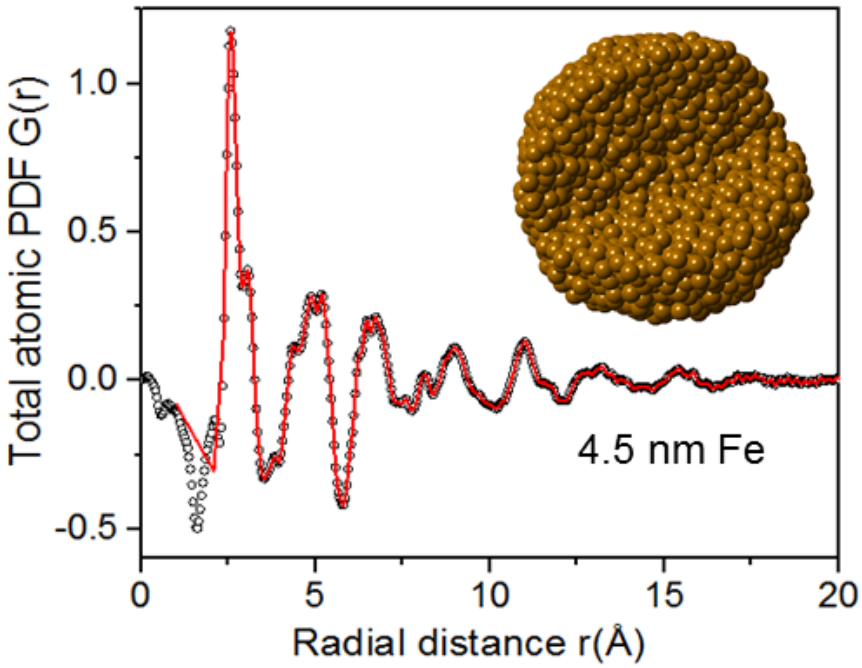

Figure S6. Experimental (symbols) and RMC fit (red line) atomic PDF for 4.5 nm pure Fe particles. The computed PDF is derived from the 3D structure shown in the inset. The structure comprises about 6000 Fe atoms and is refined against experimental PDF data through RMC as described in the text.

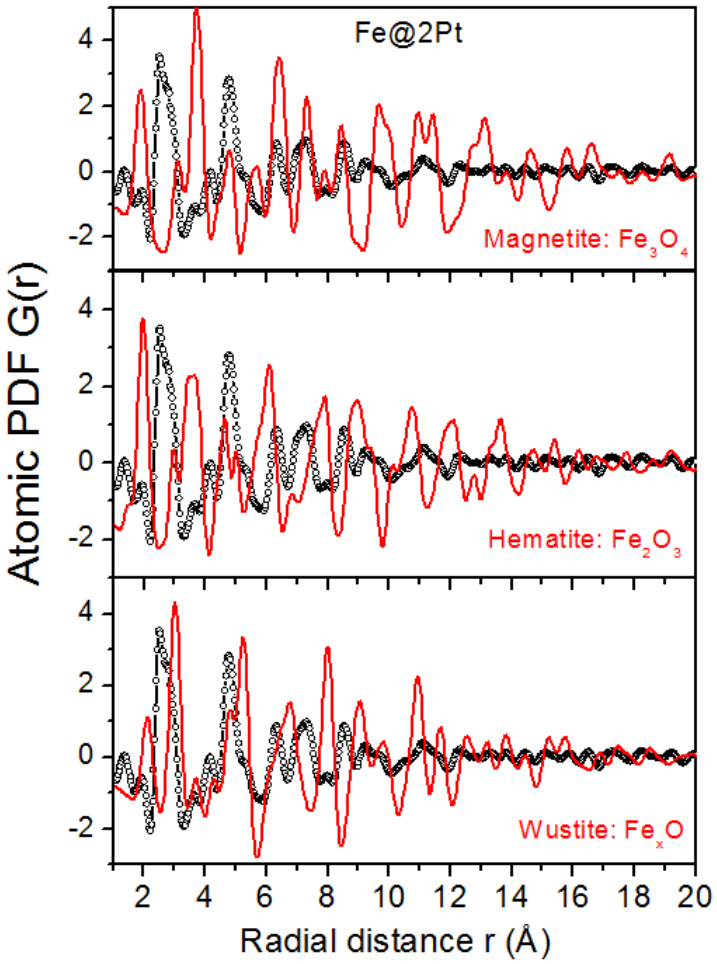

Figure S7. Experimental (symbols) Fe-Fe partial PDF for Fe@2Pt NCs and computed PDFs for common Fe^{+2} and Fe^{+3}–involving oxides, including wustite, hematite and magnetite. Experimental and computed PDF data disagree testifying to the metallic character of Fe atomic in Fe@2Pt NCs.

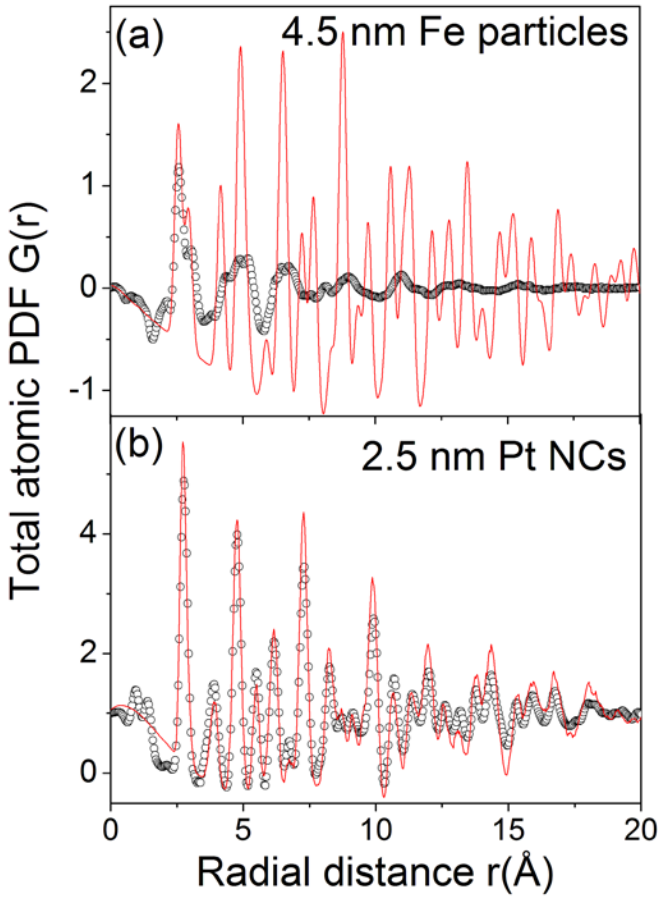

Figure S8. (a) Experimental (symbols) and computed (red line) total atomic PDFs for 4.5 nm Fe particles. The bcc-type model captures the essential structural features of the particles such as, for example, the nearly split first peak in the PDF data. The model though is well too ordered structurally, i.e. shows a sequence of very well defined atomic coordination spheres (PDF peaks), as compared to the actual Fe particles. (b) Experimental (symbols) and computed (red line) total PDFs for 2.5 nm Pt nanocrystallites. The fcc-type model reproduces the experimental data in very good detail, except in the region at higher-r values.

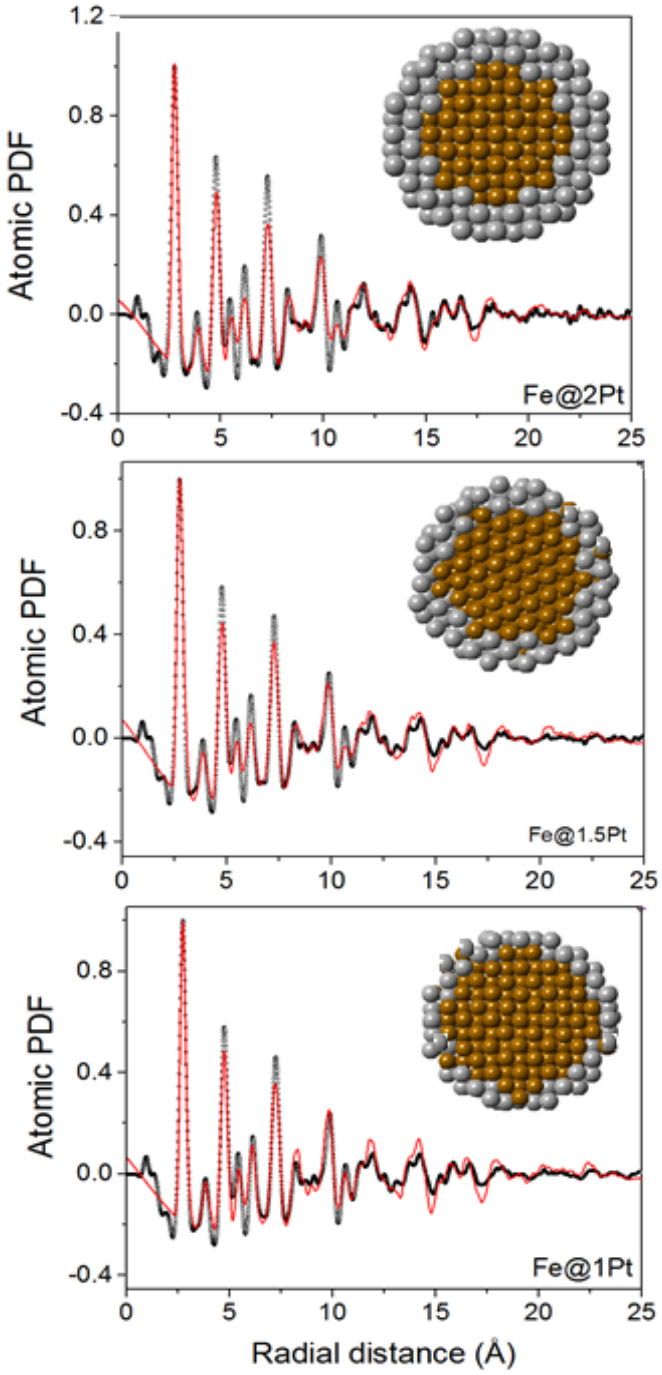

Figure S9. Experimental (symbols) and computed (red line) total atomic PDFs for Fe@Pt NCs. Computed PDFs are derived from structure models featuring a continuous fcc-type ordering throughout the NCs. The models are shown for each data set. Iron atoms are in brown and Pt atoms are in gray Peaks in the experimental and model PDFs line up in position but disagree in intensity.

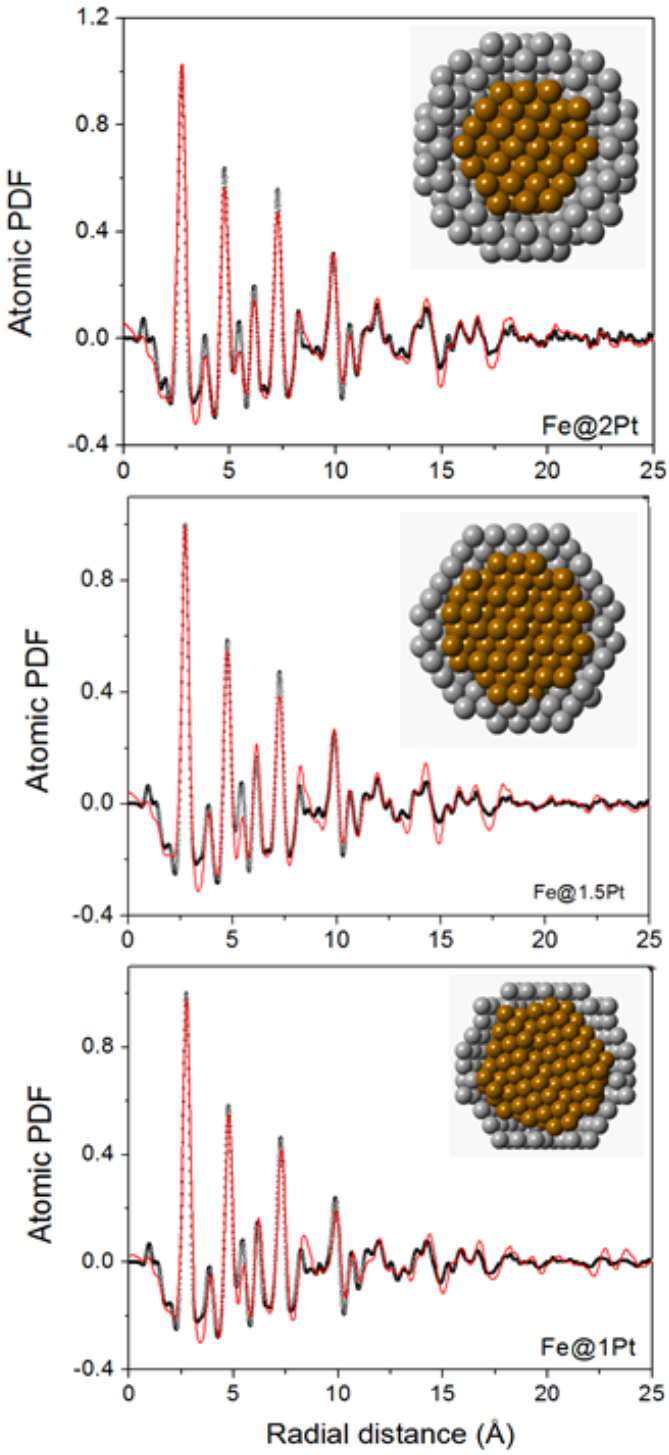

Figure S10. Experimental (symbols) and computed (red line) total atomic PDFs for Fe@Pt NCs. Computed PDFs are derived from structure models featuring a bcc Fe core nested inside fcc Pt shell. The models are shown for each data set. Iron atoms are in brown and Pt atoms are in gray. Peaks in the experimental and model PDFs agree reasonably well in both position and intensity.

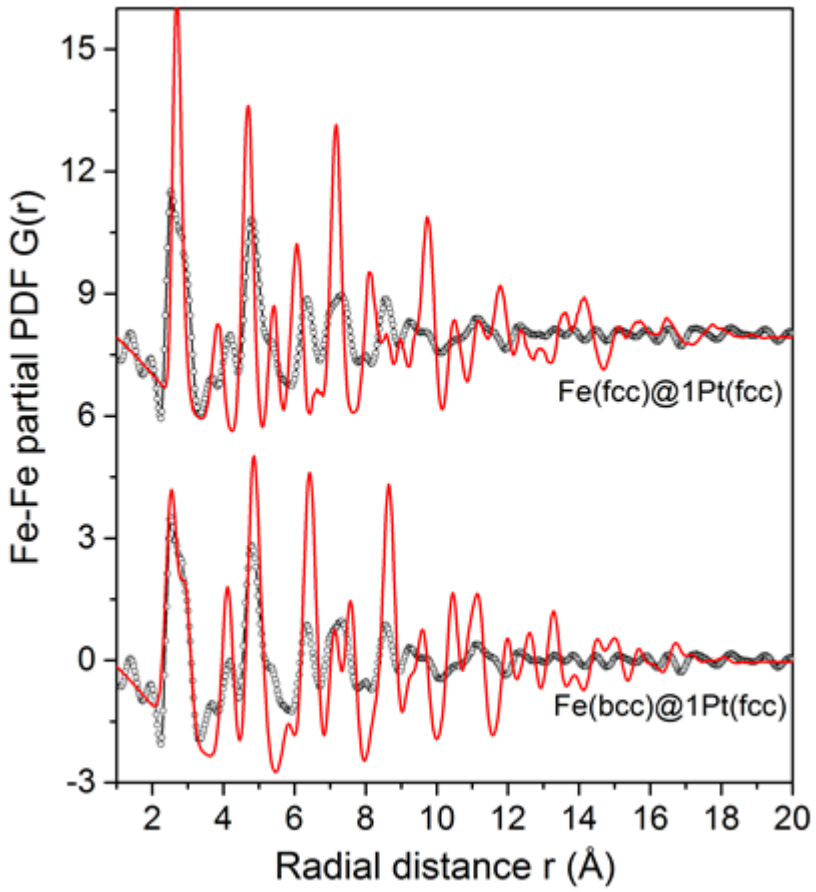

Figure S11. Experimental (symbols) and computed (red line) Fe-Fe partial atomic PDFs for Fe@1Pt NCs. Computed PDFs are derived from structure models featuring Fe(fcc)@Pt(fcc) NCs, wherein both Fe and Pt atoms are ordered fcc-like, and Fe(bcc)@Pt(fcc) NCs, wherein a bcc Fe core is nested inside a fcc Pt shell. The PDF derived from the latter model approaches the experimental data much closer than the PDF derived from the former model does it.

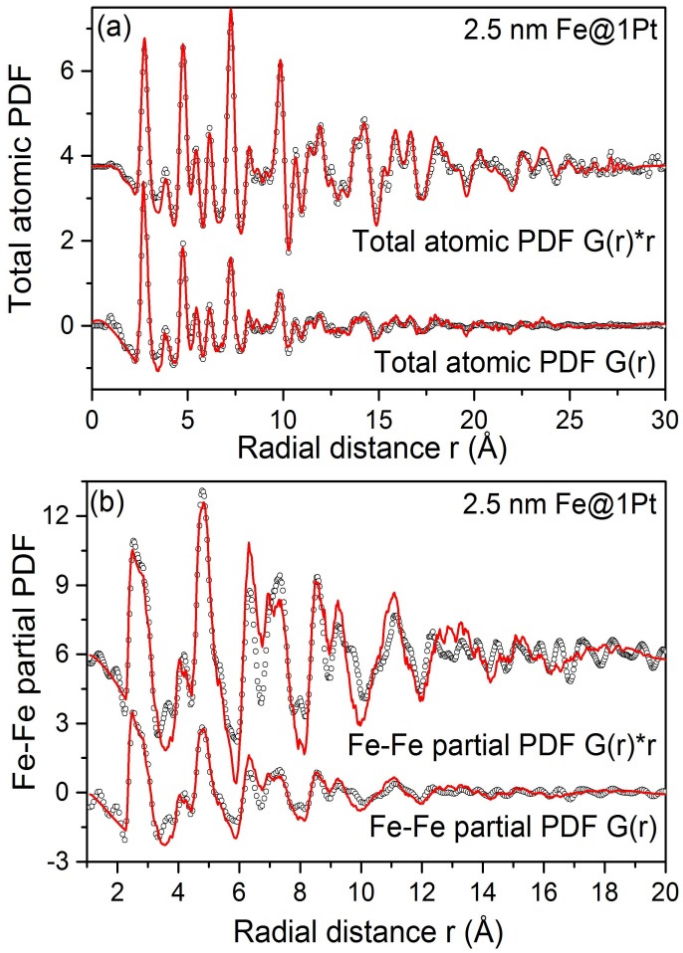

Figure S12. ***(a)*** Experimental (symbols) and RMC-fit (red line) total PDF for 2.5 nm Fe@1Pt NCs. Data are presented as G(r) and G(r)**r*, where *r* is the radial distance. ***(b)*** Experimental (symbols) and RMC-fit (red line) Fe-Fe partial PDF for Fe@1Pt NCs. Data are presented as $G_{Fe\text{-}Fe}(r)$ and $G_{Fe\text{-}Fe}(r)*r$. RMC fits in (a) and (b) reflect the respective 3D atomic structure shown in Figure 3a. As data summarized here show, RMC fits to the experimental PDF data represented in terms of G(r) are very sensitive to the short-range (lower-r PDF peaks) and not so to the longer range (higher-r PDF peaks) interatomic correlations in Fe@1Pt NCs. On the other hand, RMC fits to the experimental PDF data represented as G(r)**r* are very sensitive to the longer-range (> 10 Å) and not so to the short-range (< 10 Å) interatomic correlations in Fe@1Pt NCs. Alternating RMC refinement between fitting the same experimental PDF data represented as G(r) and G(r)**r* ensures that the refined 3D structure describes truly the interatomic correlations (atomic structure) across the studied NCs, including both the 3D structure of bcc Fe core and that of fcc Pt skin.

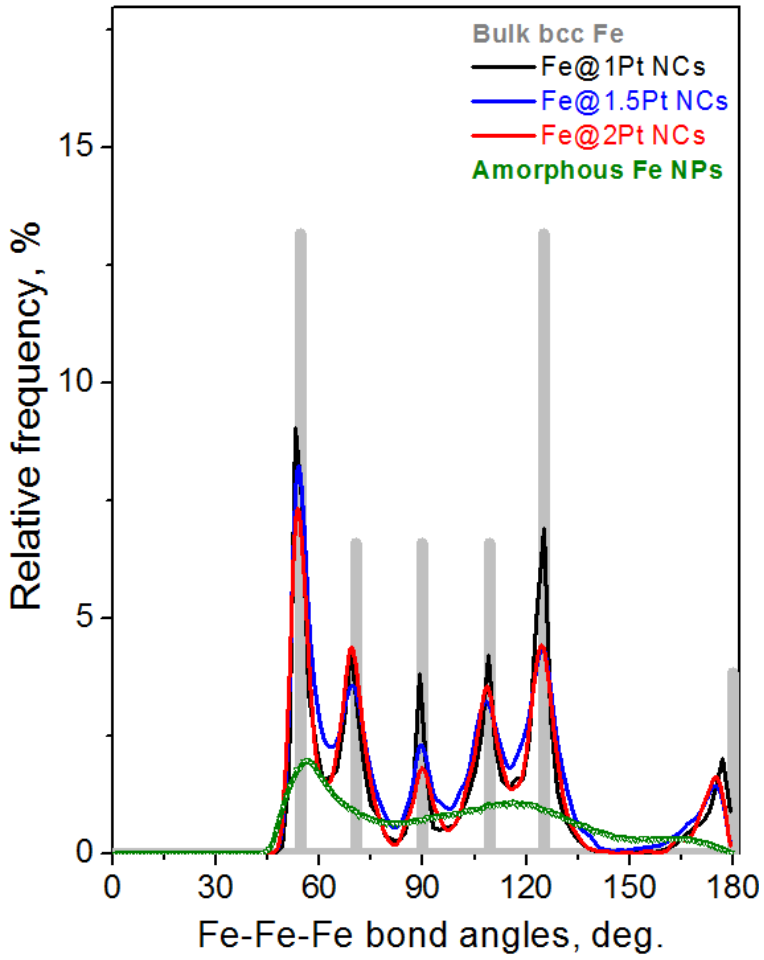

Figure S13. Distribution of bond angles in bulk bcc Fe (bars) and atoms in Fe cores of Fe@Pt NCs. Distribution of bond angles in heavily disordered 4.5 nm Fe particles is also shown for comparison.

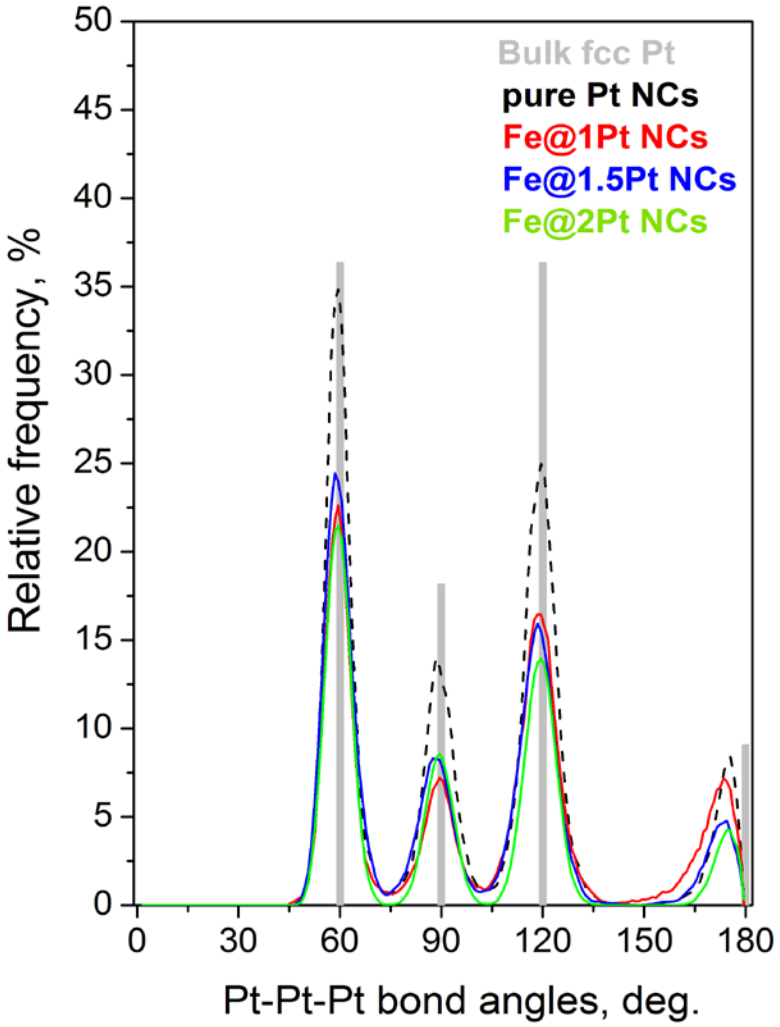

Figure S14. Distribution of bond angles in bulk fcc Pt (bars) and atoms forming the Pt skin of Fe@Pt NCs.

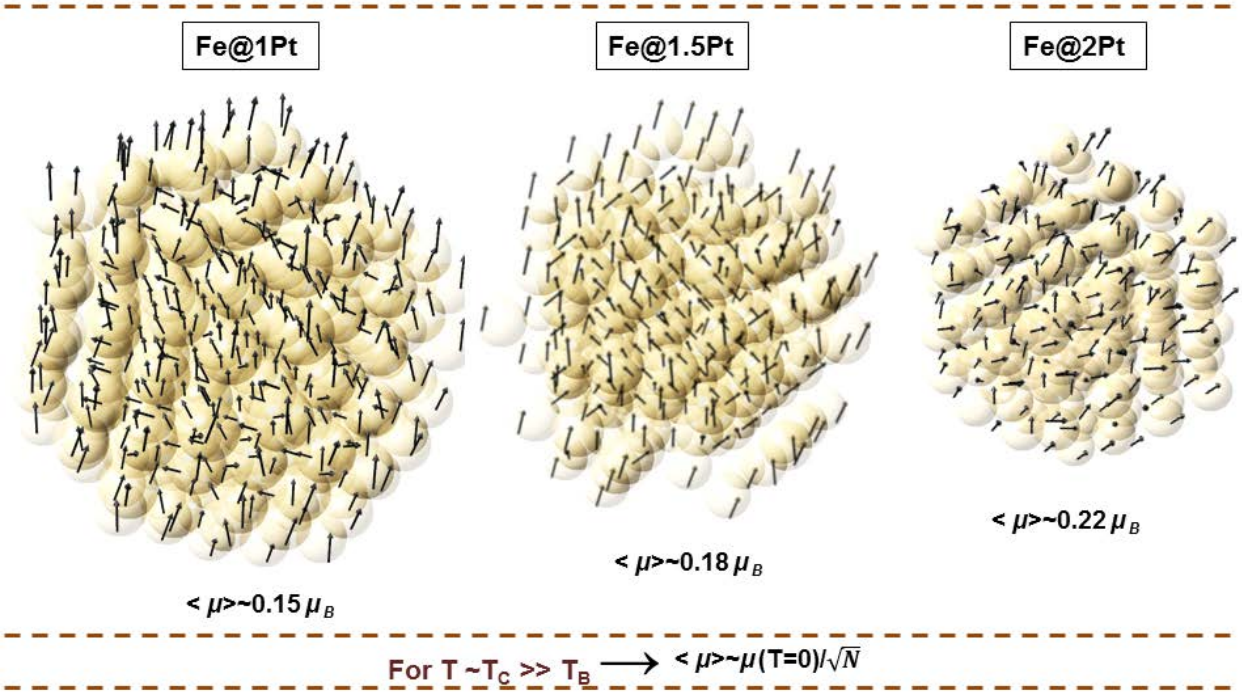

Figure S15. Atoms (circles) forming the Fe cores of Fe@Pt NCs. Arrows represent the magnetic moments of individual atoms assessed as explained in the text. The arrows point in different directions because thermal fluctuations are strong for $T \sim T_c >> T_B$, where $T_c = 1043$ K is the Curie temperature of bulk Fe and T_B is the "blocking temperature" of the respective cores. Note that finite size systems such as Fe cores may not undergo sharp magnetic order-disorder transitions with increasing temperature. Hence, the average magnetic moment, $\langle\mu\rangle$, of atoms in the cores is not "zero" but $\rightarrow \mu(T=0)/\sqrt{N}$, where N = 328, 233 and 166 for Fe@1Pt, Fe@1.5Pt and Fe@2Pt NCs, respectively.

SI REFERENCES:

S1. J.-H. Jang, E. Lee, J. Park, G. Kim, S. Hong and Y.-U. Kwon *Sci. Rep.* **3:2872** (2013).

S2. W. B. Pearson, in "*The Crystal Chemistry and Physics of Metals and Alloys*" (Wiley-Interscience: New York, 1972).

S3. C.R. Parkinson, M. Walker, C.F. McConville, *Surf. Sci*. **454** (2003) 19.

S4. D. R. Baer and M. H. Engelhard. *J. Electron Spectrosc. Rel. Phenom.*, **415** (2009) 178.

S5. T. Yamashita and P. Hayes *Appl. Surf. Sci.* **254** (2008) 2441.

S6. L. Chen, A. Yelon and E. Sacher *J. Phys. Chem.* **116** (2012) 6902.

S7. T. Toda, H. Igarashi, H. Ucida and M. Watanabe *J. Electrochem. Soc.* **146** (1999) 3750.

S8. M. Xue and Q. Guo *Chem. Phys. Lett.* **551** (2012) 92.

S9. D.–Q. Yang and E. Sacher *J. Phys. Chem C* **113** (2009) 6148.

S10. M. Peuckertand H. P. Bonzel *Surf. Sci*. **145** (1984) 239.

S11. B. R. Cuenya, J. R. Croy, L. K. Ono, A. Naitabi, H. Heinrich, W. Keune, J. Zhao W. Sturhahan, E. E. Alp and M. Hu *Phys. Rev. B* **80** (2009) 125412.

S12. P. H. Citrin and G. K. Wertheim *Phys. Rev. B* **27** (1983) 3176.

S13. Z. Bayindir, P.N. Duchesne, S. C. Cook, M. A. MacDonald and P. Zhang *J. Chem. Phys.* **131** (2009) 244716.

S14. V. Stamenkovic, B. S. Mun, M. Arenz, K. J. J. Mayrhofer, C. A. Lucas, G. Wang, P.N. Ross and N. M. Markovic *Nat. Mat*. **6** (2007) 241.

S15. J. K. Norskov, J. Rossmeisl, A. Logadottir, L. Lundkvist, J. R. Kitchin, T. Bligaard and H. Jonsson *Phys. Chem*. B ***108*** (2004) 17886.

S16. B. Hammer and J. K. Norskov *Adv. Catal*. **45** (2007) 71.

S17. V. Stamenkovic, B. S. Mun, K. J. J. Mayrhofer, P. N. Ross, M. N. Markovic, J. Rossmeisl, J. Greeley and J. K. Nørskov, *Angew. Chem. Int. Ed*. **45** (2006) 2897.

S18. F. Bodker, S. Morup and S. Linderoth *Phys. Rev. Lett.* **72** (1994) 282.

S19. I. M. L. Billas, J. A. Becker, A. Chatelain and W. A. de Heer *Phys. Rev. Lett*. **71** (1993) 4067.

S20. D. J. Sellmyer and R. Skomski (Eds.) in "*Advanced Magnetic nanostructures*" (Springer; 2005.

S21. H. Kronmüller and S. Parkin (Eds.) in "*Handbook of Magnetism and Advanced Magnetic Materials"* Vol. 3. (Wiley; 2007).

S22. D. L. Leslie-Pellecky and R. D. Rieke *Chem. Mat*. **8** (1996) 1770.

S23. O. Margeat, F. Dumestre, C. Amiens, B. Chaudret, P. Lecante, M. Respaud, *Prog. Sol. State Chem*. **33** (2005) 71.

S24. J. M. D. Coey, in *Magnetism and Magnetic Materials* (Cambridge University Press, Cambridge, 2010).

S25. E. C. Stoner and E. P. Wohlfarth, *Philos. Trans. R. Soc. London Ser. A* **599** (1948) 240.

S26. D. Tomanek , S. Mukherjee and K. H. Bennemann *Phys. Rev. B* **28** (1983) 665.

S27. J. Zhao, X. Chen, Q. Sun, F. Liu and G. Wang *Phys. Lett. A* **205** (1995) 308.

S28. T. C. Monson, E. L. Venturini, V. Petkov , Y. Ren, M. Judith and D.L. Huber *J. Magn. Mag. Mater.* **331** (2013) 156.

S29. S. D. Shastri, K. Fezzaa, A. Mashayekhi, W.-K. Lee, P. B. Fernand ez and P. L. Lee *J. Synchrotr. Rad.* **9** (2002) 317.

S30. V. Petkov. *Mater. Today* **11** (2008) 28.
S31. T. Egami and S. J. L. Billinge in "*Underneath the Bragg peaks".;* (Pergamon Press: Oxford, 2003).
S32. P. H. Fuoss, P. Eisenberger, W. K. Warburton and A. Bienenstock *Phys. Rev. Lett.* **46** (1981) 1537.
S33. V. Petkov and S. D. Shastri *Phys. Rev. B* **8** (2010) 165428:1-8.
S34. C. Wurden, K. Page, L. Llobet, C. E. White and Th. Proffen *J. Appl. Crystallogr*. **43** (2010) 635.
S35. Y. Waseda in "*Anomalous X-Ray Scattering for Materials Characterization: Atomic-Scale Structure Determination";* (Springer: Berlin, 2002).
S36. V. Petkov, S. Shastri, Sh. Shan, Ph. Joseph, J. Luo, C. J. Zhong, T. Nakamura, Y. Herbani and Sh. Sato *J. Phys. Chem. C* **117** (2013) 22131.
S37. V. Petkov, R. Loukrakpam, L. Yang, B. N. Wanjala, J. Luo, Chuan-Jian Zhong, and S. Shastri, *Nano Lett.* **12** (2012) 4289.
S38. W. B. Pearson, in "*The crystal chemistry and physics of metals and alloys"* (New York: Wiley-INTERSCIENCE, **1972**)
S39. L. Farrow, P. Juhas, J. Liu, D. Bryndin, E. Bozin, J. Bloch, T. Proffen and S. Billinge *J. Phys.: Condens.* Matter **19** (2007) 335219.
S40. S. Grazulis, D. Chateigner, R. T. Downs, A. F. T. Yokochi, M. Quiros, L. Lutterotti, E. Manakova, J. Butkus, P. Moeck and A.Le Bail *J. Appl. Cryst*. **42** (2009) 726; http://www.crystallography.net/cod/
S41. A. P. Sutton, J. Chen *Philos. Mag. Lett.* **61** (1990) 139.
S42. Y. Kimura, Y. Qi, T. Cagin and W. A. Goddard III *MRS Symp. Ser.* **554** (1999) 43.
S43. H. Rafii-Tabar and A. S. Sutton *Phil. Mag. Lett*. **63** (1991) 217.
S44**.** B. Prasai, A. R. Wilson, B. J. Wiley,Y. Ren and V. Petkov *Nanoscale* **7** (2015) 17902.
S45. W. Smith, W. C. Yong, P. M. Rodger *Molecular Simulations* **28** *(2002)* 385.
S46. Y. Nose, A. Kushida, T. Ikeda, H. Nakajima, K. Tanaka and H. Numakura, *Mat. Trans*. **44** (2003) 2723.
S47. R. McGreevy and L. Pusztai *Molec. Simul.* **1** (1998) 359.
S48. X. Hua, Z. Liu, P. G. Bruce and C. P. Grey *J. Am. Chem. Soc.* 137 **(2015)** 13612.
S49. K. M.Ø. Jensen, P. Juhas, M. A. Tofanelli, C. L. Heinecke, G. Vaughan, G. C. J. Ackerson and S. J. L. Billinge *Nat. Comm*. **7** (2016) 11859.
S50. K. Kodama, S. Iikubo, T. Taguchi and S. Shamoto *Acta Cryst*. **A62** (2006) 444.
S51. K. Page, Th. Proffen, H. Terrones, M. Terrones, L. Lee, Y. Yang, S. Stemmer, R. Seshadri and A. K. Cheetham *Chem. Phys. Let*. **393** (2004) 385.
S52. S. Zhen and G. J. Davies *Phys. Stat. Sol*. **78a** (1983) 595.
S53. V. Petkov, B. Prasai, Y. Ren, S. Shan, J. Luo, P. Joseph and C.-J. Zhong *Nanoscale* **26** (2014) 10048.
S54. O. Gereben and V. Petkov *J. Phys.: Condens. Matter* **25** (2013) 454211:1-9.
S55. B. H. Toby and T. Egami *Acta Cryst. A,* **48** (1992) 336.
S56. L. B. Skinner, C. Huang, D. Schlesinger, L. G. M. Petterson, A. Nillson and C. J. Benmore *J. Chem. Phys*, **138** (2013) 074506.
S57. B. E. Warren, in "*X-ray Diffraction*" (Addison-Wesley Publ. Co; **1969**).
S58. X. Xu, Sh. Yin, R. Moro, A. Liang, J. Bowlan and W. A. de Heer *Phys. Rev. Lett*. **107** (2011) 057203.
S59. O. Sipr, M. Kosuth and H. Ebert *Phys. Rev. B* **70** (2004) 174423.

S60. F. Aguilera-Granja, J. M. Montejano-Carrizales, J.L. Moran-Lopez *Phys. Lett. A* **242** (1998) 255.
S61. Y. Xie and J. A. Blackman *J. Phys.: Condens. Matter* **15** (2003) L615.
S62. P. J. Jensen and K. H. Bennemann Z. Phys. D 35 (1995) 273.
S63. F. Reif in *Fundamentals of Statistical and Thermal Physics*. McGraw–Hill (1965).
S63. Ch. Kittel in *Introduction to Solid State Physics (4th ed.).* New York: John Wiley & Son (1971).
S64. L. M. Falicov and G. A. Samurjai *Proc. Natl. Acad. Sci*. **82** 1985 2207.
S65. Ch. Y. Yang, K. H. Johnson, D. R. Salahub, J. Kaspar and R. P. Messner Phys. Rev. B 24 (1981) 5673.
S66. Isabelle M.L. Billas, A. Chatelain and Walt A. de Heer *Science* **265** (1994) 1682.
S67. X. Ma and H. Xin, *Phys. Rev. Lett.* **118** (2017) 036101-1.
S68. F. Calle-Vallejo, J. Tymoczko, V. Colie, Q. H. Vu, M. D. Pohl, K. Morgenstern, D. Loffreda, Ph. Sautet, W. Schuhmann and A. S. Bandaenka *Science* **350** (2015) 185.
S69. P. Bobadova-Parvanova, K.A. Jackson, S. Srinavas, M. Horoi, C. Kohler and S. Seifert *J. Phys. Chem. Phys.* **116** (2002) 3576.
S70. H. Zhi-Gao, Ch. Zhi-Gao and J. Li-Quin *Chinese Phys.* **15** (2006) 1602.
S71. J. A. Franco, A. Vega and F. Aguilera-Granja *Phys. Rev. B* **60** (1999) 434.
S72. K. W. Jacobsen, P. Stolze and J. K. Norskov *Surf. Sci.* **366** (1996) 394.
S73. S. M. Foiles, M. I. Baskes and M. S. Daw *Phys. Rev. B* **33** (1986) 7983.
S74. R. Ferrando, J. Jellinek and R. L. Johnston *Chem. Rev.* **108** (2008) 846.
S75. X. Xu, Sh. Yin, R. Moro and W. A. de Heer *Phys. Rev.* **B 78** (2009) 054430.